Arbeitsbericht

MeteoSchweiz
MétéoSuisse
MeteoSvizzera
MeteoSvizra
MeteoSwiss

Autoren
Sandro Buss
Eric Jäger
Christoph Schmutz

210 Evaluation of turbulence forecasts with the aLMo

Arbeitsbericht

MeteoSchweiz

Nummer: 210

Autoren
Sandro Buss
Eric Jäger
Christoph Schmutz

Evaluation of turbulence forecasts with the aLMo

Bestelladresse:
Bundesamt für Meteorologie und Klimatologie (MeteoSchweiz)
Office fédéral de météorologie et de climatologie (MétéoSuisse)
Ufficio federale di meteorologia e climatologia (MeteoSvizzera)
Uffizi federal per meteorologia e climatologia (MeteoSvizra)
Federal Office of Meteorology and Climatology (MeteoSwiss)

MeteoSchweiz
Krähbühlstrasse 58
Postfach 514
CH-8044 Zürich

Telefon +41 44 256 91 11
Telefax +41 44 256 92 78
info@meteoschweiz.ch
www.meteoschweiz.ch

Evaluation of turbulence forecasts with the aLMo

Table of contents

1. Introduction

«Le système étant excité par de légères variations, ne s'écartera pas sensiblement du lieu qu'il occupait d'abord.»
Baron J. Fourier

High altitude clear-air turbulence (CAT) remains a significant forecast problem for aviation. The number of fatal accidents involving CAT encounters by jet aircraft is relatively low though, but serious injuries have occurred, especially when severe CAT is encountered suddenly and unexpectedly and passengers have unfasten seat belts. CAT phenomena are therefore of high practical importance for air traffic; air transport companies have a vital interest in receiving early warnings of likely CAT areas. It is a matter of passenger comfort and safety as well as aircraft safety. In cases of severe or extreme CAT, structural damage to aircraft may result. Aircraft material fatigue arising from severe CAT can reduce lifespan of airplanes and hence be of high economic importance. There is also a significant increase in fuel consumption during turbulent flights (Ellrod and Knapp, 1991).

In the framework of the ICAO WAFS (world area forecast system) standardized turbulence forecast is currently provided for the whole aeronautical community. This kind of forecast bases on global models which are run for the two WAF-Centers in Exeter (UK) and Washington (USA). Global models do not resolve accurately the complex topography of the Alps, therefore, in this study we aim to to evaluate turbulence forecasts based on outputs of a high resolution model, the aLMo (alpine model), in the wider region of the alps where a sinificant influence of the topography is expected.

A second more indirect motivation is to determine how good gravity waves (GWs) and wave breaking are represented in the resolved flow of various meteorological parameters within a mesoscale numerical model as the aLMo from MeteoSwiss. The reason is that GWs play an important role as a source of turbulence. Essential questions might be about phase errors, model numerics, i.e. what the response of the model is to what could be a turbulent event; or whether the eddy diffusion system counter-balances the development of turbulent motion.

Turbulence is a small scale meteorological hazard that was studied extensively in the 1950s and 1960s. Turbulence refers to motions at various intensities and scales in three dimensions and so a complete description of it would be expected to be complex. However over a certain range of eddy sizes, the inertial subrange, defined in the similarity hypothesis of Kolmogorov (1941) all the statistical properties of atmospheric turbulence can be related to one parameter, ε, a dissipation rate of turbulent energy, the eddy dissipation rate (EDR).

It fortunately turns out that this inertial subrange includes those gusts which are of primary importance for many aircraft's gust loads, for aircraft fatigue problems, and for the qualitative human "feel" of turbulence in flight, say order 100 m or so. Any turbulence measurements, no matter how accurate, can only be related to other conditions, forecasts, or designs in a somewhat qualitative sense because of the complex distributions and random nature of turbulence. Within this fundamental restriction, the relations are made most quantitative by the broad use of a simple concept, the similarity hypothesis of Kolmogorov (1941). The simplicity of the suggested standardization principle is perhaps its greatest virtue; the technique is simple enough to permit routine handling of varying complex data.

Several theoretical and experimental studies on possible mechanisms of turbulence production have been published. A main emphasis has been on the various ways in which gravity waves might produce turbulence, and some review has been summarized e.g. by Bretherton (1969) and Scorer (1968) who has also proposed mechanisms by which the gravity waves themselves are generated.

Gossard and Hooke (1975) review the following mechanisms that can act as energy sources for gravity waves: convection, density impulses (accelerating fronts), geostrophic or ageostrophic adjustment, topographical forcing and vertical shear instability. Several articles report observations of inertia GW which could be attributed to emanate from vertical shear instabilities, e.g. Thomas et al. (1999); Pavelin et al. (2001); Hertzog et al. (2001); Peters et al. (2003), Shibata et al. (2003), Hitchman et al. (2003) and Buss et al (2003). Thus, shear instability might be a direct source of turbulence, when the static stability is small in comparison with or an indirect source as the shear instability radiates gravity waves which whether may trigger further Kelvin Helmholtz instability (KHI) in neighboring layers (Roach, 1970) or via the breaking of the generated GWs.

Dutton and Panofsky (1970) review the following relevant facts concerning the regions where and when clear air turbulence occurs:

i) The probability that clear air turbulence will occur is largest in regions of strong vertical wind shear (leading to Kelvin-Helmholtz instability) and strong horizontal temperature gradients. (These two factors are closely related to each other, because the wind tends to change in the vertical most rapidly when there are strong horizontal temperature gradients.)
ii) In middle latitudes, clear air turbulence is most frequent and most severe in January and February, because in these months horizontal temperature gradients in the upper atmosphere are the largest.
iii) The probability of an airplane encountering clear air turbulence increases with increasing altitude, reaching a maximum at the general region of the boundary between the troposphere and the stratosphere. This boundary, called tropopause, is associated in middle latitudes and in the subtropics with the atmospheric jet stream, a region of strong winds which circles the globe in a sinuous pattern. Clear turbulence also occurs in the stratosphere, above this region of maximum winds, but less frequently.
iv) Clear air turbulence is more frequent and more intense over land than over the oceans, and over mountains and hilly terrain than over plains.
v) Clear air turbulence is likely to occur in regions in which the Richardson number (see Section 6.6) is small.

Particular reference has been made to Kelvin-Helmholtz instability (see picture on page 1, e.g. Roach, 1970), which is perhaps the principal mechanism found to be responsible for CAT and maybe the only transition mechanism for which there is reasonable agreement between theory (e. g. Miles and Howard, 1964) and observations in the laboratory (e.g. Thorpe, 1968), the atmosphere (Ludlam, 1967) and the ocean thermocline (Woods, 1968). KHI is a phenomenon that resembles a breaking ocean wave. KHI occurs when vertical wind shear within a stable layer exceeds a critical value. The presence of these strongly sheared regions is often marked by billow wave-cloud formations that are sometimes observed by satellite imagery, radar or by eye. Roach (1970) supposes that KHI is the major mechanism of transition from laminar to turbulent flow in free shear layer in the atmosphere and proposes the following sequence of events during this process:

vi) The value of Ri_L (layer Richardson Number, definition see Section 6.6, Equation (15), with vertical dimension small compared to the frontal thickness) for an inviscid shear layer falls below 0.25.
vii) The resultant KHI develops two-dimensional rolls aligned along the (horizontal) vorticity vector, which entrain fluid from above and below the original shear layer.
viii) The rolls break up into general turbulence within a layer about four times the thickness of its undisturbed value.
ix) This results in a concentration of static stability at the boundaries of the turbulent layer, but not apparently of vertical wind shear. This strongly suggests that turbulence itself plays a part in producing the layered structure of the atmosphere.
x) The interface between turbulent and non-turbulent fluid radiates gravity waves which may trigger further KHI in neighboring layers.
xi) The gradient Richardson number, defined in Section 6.6, Equation (14), within the layer will become very small as turbulence produces a nearly adiabatic lapse rate, but does not smooth

out the velocity shear (although it may reduce it). However, Ri_L may increase to about unity as the original vertical wind and potential temperature gradients will not be much changed.

xii) This turbulent layer will decay unless the large-scale deformation processes can reduce Ri_L to its critical value on a time scale comparable to the decay time scale.

Thus it seems likely that there will at first be scattered patches of KHI occurring in layers of widely varying thickness. If the deformation processes intensifies, these patches will presumably become more frequent and thicker (with resultant radiation of GW) and may eventually merge to form a continuous layer of turbulence. At this stage the time for a given air parcel to pass through a turbulent region is long compared to the natural decay time of the turbulence (of order (vertical shear)$^{-1}$), which is now being maintained against dissipation by the large-scale deformation.

It would then appear that the principal effect of turbulence is to prevent deformation processes reducing Ri_L below some limiting value. It is further possible that the profiles of wind and temperature through the turbulent layer have become self-maintaining, and that the thickness of the turbulent layer has ceased to change rapidly.

Surface roughness and its spatial variations are a third cause of turbulence, affecting the planetary boundary layer but not higher altitudes.

In the present study, the different sources of turbulence are not dissociated. The expectation is that an aLMo turbulence indicator or the linear, non-linear or probabilistic combination of several aLMo indicators will suffice to accurately forecast turbulence of any source so ever. Therefore neither terrain induced turbulence nor mountain induced turbulence are specifically accounted for, despite the numerous literature on the topic (Reiter and Foltz, 1967; Hopkins, 1977; Bacmeister et al., 1994; Kim and Arakawa, 1994; Turner, 1999; McCann, 2003; Eidsvik et al 2004; etc).

Since the longterm strategic vision of MeteoSwiss is to become the competence center for alpine meteorology and climatology (CC ALPMET), this work was funded through research and development (R&D) of MeteoSwiss. It was accomplished at the aeronautical MET department "Flugwetter" at Zürich intl. airport. The time frame for this study was confined to 7 months, this study therefore does not claim for completeness (see e.g. Section 6.12). The approach followed at the National Center for atmospheric research (NCAR) e.g., developing an integrated turbulence forecasting algorithm (ITFA) would go beyond the scope of this analysis. The heart of the ITFA concept is that several algorithms for diagnosing turbulence potential with results combined in some intelligent way can provide better forecasts than a single algorithm (Sharman et al., 2000).

This paper is organized as follows. In Section 2 the observational data are described then the methodology of deriving turbulence intensities from those observations is introduced. In the following Section, the limited-area model and its setup are presented. In Section 5 a short validation of the mesoscale model is undertaken. Then the turbulence indicators from the numerical forecast model are introduced in Section 6, correlated with observations, and finally in Section 8 ranked. In the final Sections, some recommendations are delivered and some summarizing remarks conclude the study.

2. Airborne measurements

In the following subsections we shortly present the two data sources employed for the present study.

2.1 MAP data

During the field phase of the Mesoscale Alpine Program (MAP), scheduled from August 15th to November 15th 1999, a very large experimental effort over the whole mountain range of the Alps was made. Thanks to the active international cooperation, a number of high technology atmospheric and hydrological probing facilities were available, and their optimal use had been discussed and planned in

advance, in relation to the potential weather situations and with a hierarchy of well-defined scientific objectives. Among them, one was to improve the understanding of three-dimensional gravity wave breaking and associated wave drag in order to improve e.g. the parametrization of gravity wave drag effects in numerical weather prediction and climate models. Therefore, some intensive observations periods (IOP 2, 8, 13, 15 and 16) were dedicated to observe breaking gravity waves and the MAP aircrafts were seeking turbulent flow regions. All observations are available with a time-resolution of one second.

The deployed aircrafts during MAP were the Arat and Merlin (Météo France), the C-130 (UK), the Dornier (A), the Falcon (DLR), the Metair (CH), the Electra (NCAR) and the P-3 (NOAA).

Data from the vertical accelerometers of the MAP aircrafts were retrieved as long as they were available. This was the case for the Falcon, the P-3, the Electra and the Dornier but not for the Arat, the C-130 and the Merlin. As can be seen from Figures 4 and 5, the vertical accelerometers are specific to each aircraft.

Wide documentation on MAP and all available measurements can be downloaded at www.map.ethz.ch and www.map2.ethz.ch.

2.2 Swiss data

Flight Data Monitoring (FDM) programs assist an operator to identify, quantify, assess and address operational risks. Since the 1970's the Safety Regulation Group (SRG) has helped develop and support such systems and used FDM information to support a range of airworthiness and operational safety tasks. Through this co-operative development work many farsighted operators have demonstrated the safety benefits of FDM such that the International Civil Aviation Organization (ICAO) have recommended their use for all Air Transport operations in aircraft of over 20 tons maximum weight. Further, ICAO is making FDM a standard for all such operations of aircraft over 27 tons with effect on 1st January 2005.

In such an FDM program there are typically two to three thousand parameters available. On March 11th 2004 a significant amount of turbulence reports over the Alps were transmitted by pilots to the meteorological watch office at Zürich intl. airport. Therefore, MeteoSwiss bought data from Swiss international airlines for 148 flights from and to Zürich on that day. The following parameters were acquired: UTC time, longitude, latitude, altitude of the aircraft, pressure, temperature, wind speed, wind direction and two different vertical accelerometers recordings. The delivered observations were lower bounded at 10000 ft. Note that these turbulence reports lead to turbulence warnings via SIGMET on that day. As far as possible, commercial aircrafts try to avoid turbulent levels and regions with help of these SIGMET warnings.

No documentation, neither for the Swiss data nor for the MAP data was available on the way the vertical acceleration was measured and processed.

When an aircraft penetrates a zone of developed turbulence, it experiences bumps. With accelerometers mounted in certain points of the air frame, and knowing the response functions for these points, it is possible to transform the recorded loads into atmospheric gusts of vertical winds. But in the present case, the vertical accelerations were mostly given in units of *g*, the acceleration of gravity.

Note further that the aLMo simulations corresponding to the MAP data were computed with an output of every hour while the simulations corresponding to the Swiss data have an output resolution of 3 hours.

3. Turbulence intensities from observations

«C'est ainsi qu'au défaut de nos sens, le calcul seul nous avertirait de la coexistence des vibrations simples, et, si l'on veut parler ainsi, de la composition harmonique des oscillations.»
Baron J. Fourier

Generally in meteorology and in order to derive turbulence intensities in particular, one might be curious about how much of the variance of a time series is associated with a particular frequency *f*, without regard to the precise phase of the waves. Indeed for turbulence, we anticipate that the original signal is not physically like waves at all, but one still finds it useful to break the signal into components of different frequencies that we like to associate with different eddy sizes. Therefore the essential and powerful Fourier transform is required which switches form the time space to the frequency space (the corresponding algorithm is called FFT, for fast Fourier transform) or in other words the time series *f(t)* into the frequency series *F(f)*:

$$F(f) = \int_{-\infty}^{+\infty} f(t) e^{2\pi i f t} dt \quad (1)$$

As we are interested on how much power is contained in the frequency interval between *f* and $f + \delta f$, we do not distinguish between positive and negative *f*, but rather regard *f* as varying from 0 ("zero frequency") to $+\infty$. We therefore define the one-sided power spectral density. The square of the norm of the complex Fourier transform for any frequency *f* is (Stull, 1988):

$$\|F(f)\|^2 = \left(F_{real\ part}(f)\right)^2 + \left(F_{imag.\ part}(f)\right)^2 \quad (2)$$

When $\|F(f)\|^2$ is summed over the discrete frequencies *f=1* to *N-1*, the result equals the total biased variance of the original time series and can be interpreted as the portion of variance explained by waves of frequency *f*.

Spectral theories are formulated in wavenumber space, whereas most measurements are performed in time or frequency space. To convert spatial scales to frequency scales we invoke Taylor's frozen turbulence hypothesis:

$$\kappa = \frac{2\pi f}{\bar{u}} \quad (3)$$

where $\bar{u}$ denotes the mean of the considered wind component and κ the wavenumber. The hypothesis asserts that turbulence might be seen as frozen as it advects past a sensor, i.e. the eddy will not change its properties during the measurement. This permits to switch from the period domain of the eddies to the wavenumber domain.

Since the early fourties and for several decades, such power spectra of wind velocities were already computed. A large spectral gap was then found at frequencies of about one cycle per hour, just between two energy maxima which correspond to different meteorological features (Van der Hoven, 1957). Since then, always based on the existence of such a gap, this research topic gained importance by its significant applications, but almost exclusively in the high frequency, or low period, or small wavenumber, domain maximum. One of the most important applications is the one of subgrid simulation of turbulence in weather forecast models. Van der Hoven (1957) found a local maximum in his spectra computed with wind measurements made between 91 and 108 meters height above ground level at a period of 12 minutes, corresponding to turbulence. He also observed a spectral gap at about 1

cycle/hour. This corresponds to the range where there is no physical process which could support eddy energy in the atmosphere.

As mentioned in the introduction, turbulence refers to motions at various intensities and scales in three dimensions and so a complete statistical description of it would be expected to be complex. However, over a certain range of eddy sizes, the inertial subrange defined in the similarity hypothesis of Kolmogorov (1941), all the statistical properties of atmospheric turbulence can be related to one parameter, ε, a dissipation rate of turbulent energy (the rate at which the turbulent energy is converted into heat for steady turbulence).

Kolgomorov, who first conceived the idea of an inertial subrange separating the energy-containing (production) and dissipation ranges, argued from dimensional considerations that *E(k)* in this region should be proportional to $\varepsilon^{2/3}\kappa^{5/3}$ (Kolmogorov, 1941), where κ is the wavenumber and ε the eddy dissipation rate. The *u* spectrum, see also Figure 1, in its one-dimensional form becomes

$$E_u(\kappa) = \alpha_1 \varepsilon^{2/3} \kappa^{-5/3} \quad (4)$$

where α_1 is the Kolmogorov constant with a value estimated between 0.5 and 0.6 for the *u* component. Equation (4) is the well-known -5/3 power law for the inertial subrange; see Figure 1 for a schematic illustration. In the inertial subrange, "middle" size eddies are affected neither by viscosity nor by the generation of turbulent kinetic energy. These eddies get their energy inertially from the larger-size eddies, and lose it the same way to smaller-size eddies. For a steady state turbulent flow, the cascade rate of energy down the spectrum E_i (where $i=u,v,w$), must balance the dissipation rate at the smallest eddy size, which is expressed in Equation (4).

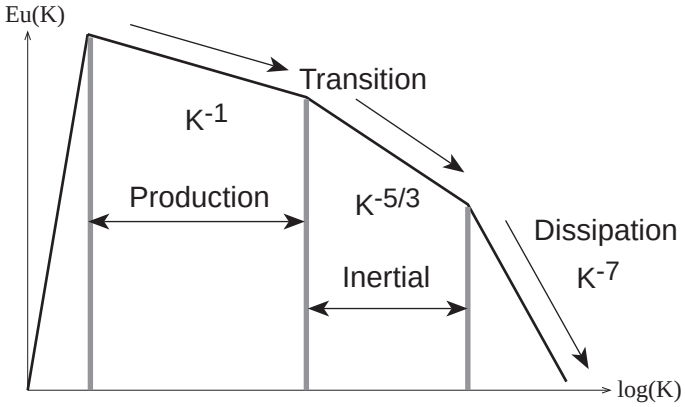

Figure 1: Theoretical power spectrum with power laws for the production, inertial and viscous dissipation ranges of the *u* component for the turbulent flow domain (from Katul and Chu 1998, with friendly permission).

MacCready (1964) proposed an alternative formulation of Equation (4), a universal turbulence standardization technique which is based quantitatively on the free atmospheric turbulence itself. It provides a single turbulence intensity number (proportional to $C_2\varepsilon^{2/3}$, where C_2 is set at 0.15):

$$E(f) = C_2 U^{2/3} \varepsilon^{2/3} f^{-5/3} \quad (5)$$

where *U* denotes the mean aircraft speed. This formulation was not applied in the present study.

Theoretical arguments suggest that turbulence is isotropic in the inertial subrange. Local isotropy implies that the velocity field is independent of rotation and reflection about the spatial axes. Even though isotropy does not apply to the energy-containing eddies, we can assume that the small-scale structure is effectively isotropic. This local isotropy is important for the derivation of small-scale

turbulence statistics. If local isotropy exists in the inertial subrange, we have the following relationship among the *u*, *v* and *w* spectra (Kaimal and Finnigan, 1994):

$$E_v(\kappa) = E_w(\kappa) = \frac{4}{3} E_u(\kappa) \quad (6)$$

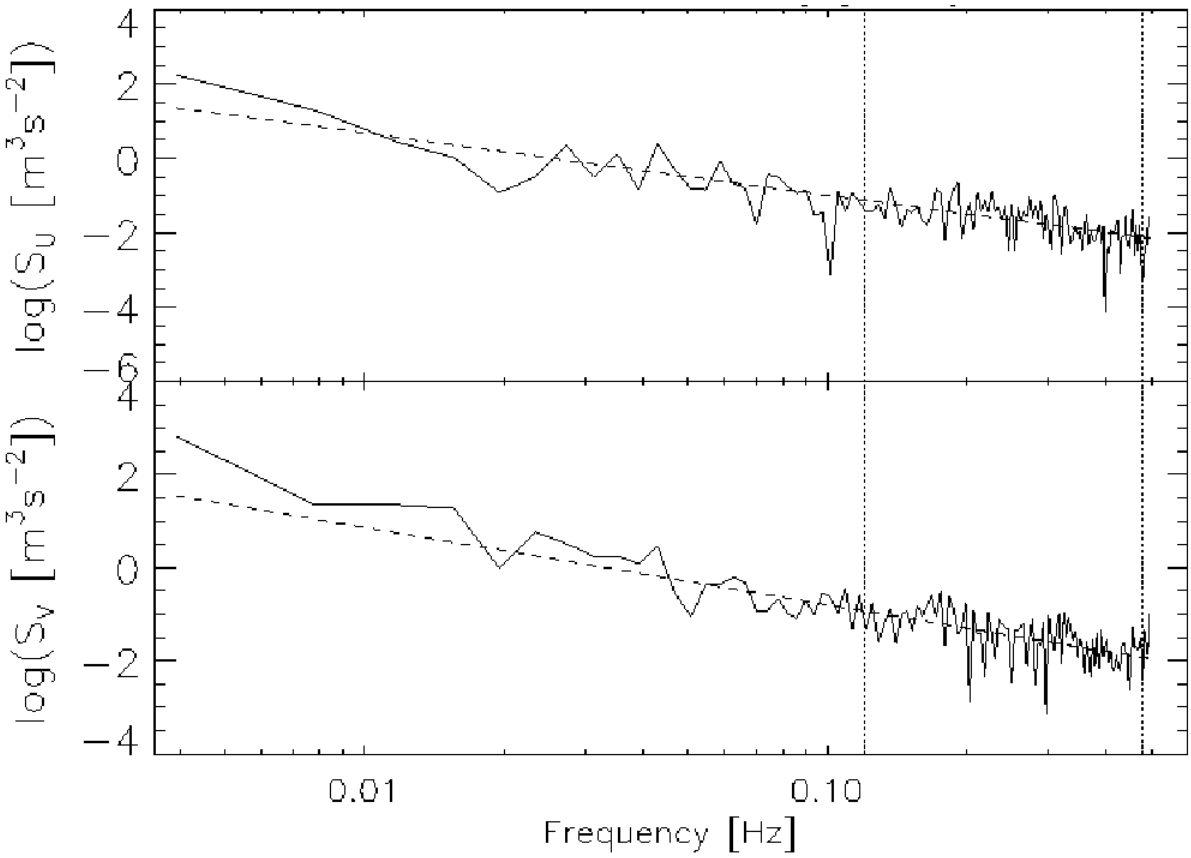

Figure 2: Power spectra of zonal (upper panel) and lateral wind components, of a Swiss flight, for 256 observations starting from 37516 s UTC, 11th of March 2004. The "inertial subrange" was arbitrarily defined between the two vertical dotted lines, 0.12 and 0.48 s^{-1}. Data in this interval was utilized to compute ε. The dashed line represents $\log(\alpha_1 * (2*\pi*f/\bar{u})^{-5/3} * \varepsilon^{2/3})$ and is therefore proportional to $\kappa^{-5/3}$.

For the graphical representation of the spectral density, we choose a log-log plot which allows a wide range of frequencies and spectral densities to be displayed (see e.g. Figure 1, 2 and 3). Also, any power law relationships between $\|F(f)\|^2$ and f appear as straight lines on this graph. $\|F(f)\|^2$ is proportional to $f^{5/3}$ in the inertial subrange portion of the spectrum, which will appear as a straight line with -5/3 slope on a log-log graph (see dashed lines on Figures 2 and 3). Unfortunately, the area under the curve is not proportional to variance as would be on a linear-linear representation.

The exact procedure applied to compute the power spectral densities as plotted in Figures 2 and 3 is as follows:

$$S_U = \frac{1}{N} u(f) \cdot \hat{u}(f) \quad (7)$$

where $\hat{u}(f)$ denotes the complex conjugate of $u(f)$ which was computed following Equation (1) and the sample size was arbitrarily chosen to be, N=256. To compute the Eddy dissipation rate, ε, following equation was then adopted:

$$\varepsilon = \left(2\pi \frac{f_i}{\overline{u}} \right)^{5/2} \cdot \alpha_1^{-3/2} \cdot S_i^{3/2} \quad (8)$$

where the i=1…N values of the zonal and of the meridional wind component were averaged separately and subsequently, the average of the two mean values was built. Therefore, every 256 wind observation pairs lead to one eddy dissipation rate value, which is representative for scales comprised between 250 m and 6.4 km (assuming an aircraft cruise of 900 km/h). Figure 2 and Figure 3 show such spectra for both horizontal wind components. The derived EDR value for the flight segment of Figure 2 is of ε_u=0.004 m^2s^{-3} and ε_v=0.008 m^2s^{-3} leading to an average value of ε=0.006 m^2s^{-3}. The corresponding EDR values from Figure 3, the measurements of which start about 13 min later are of ε_u=0.3191 m^2s^{-3} and ε_v=1.339 m^2s^{-3} leading to an average value of ε=0.829 m^2s^{-3}.

Now, following basically the ICAO recommendations, it is possible to classify the EDR (eddy dissipation rate) values in five turbulence intensities as shown in Table 1, leading for the spectra shown in Figure 2 to NIL turbulence and for Figure 3 to EXTREM turbulence.

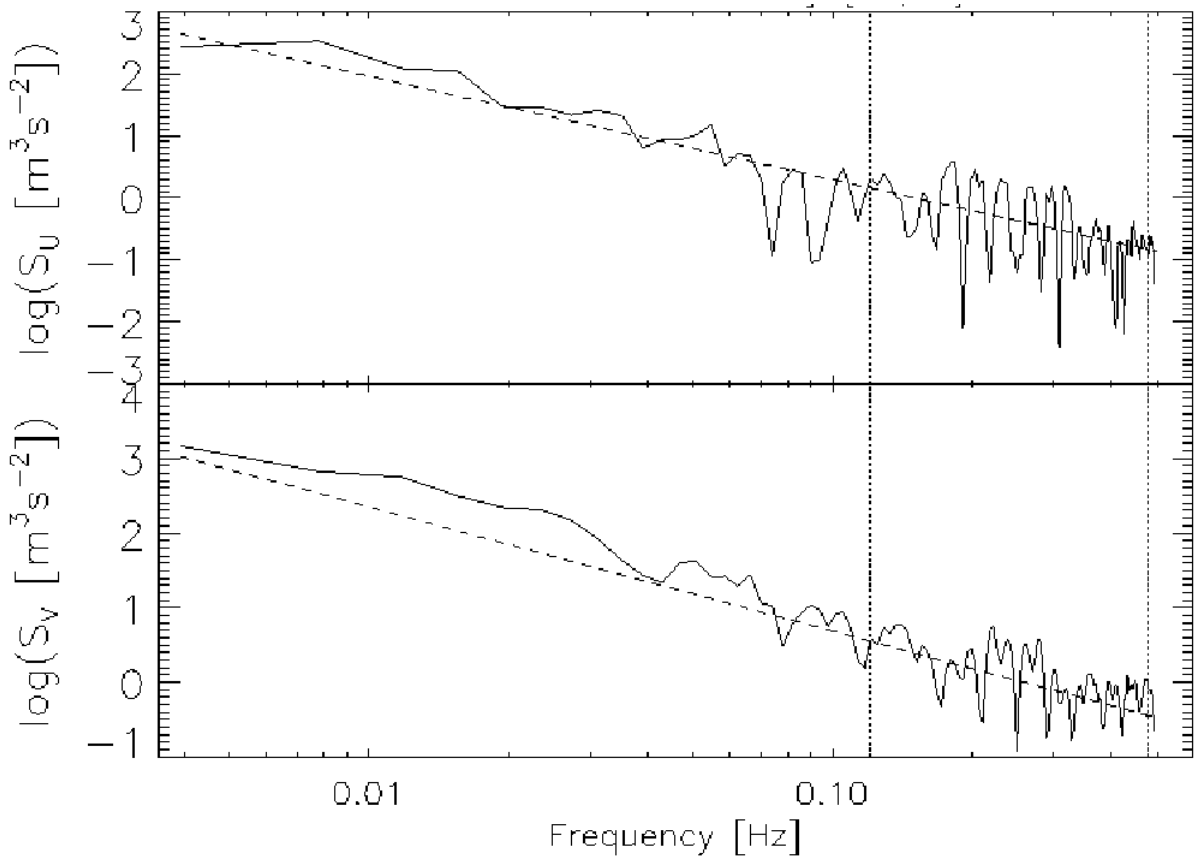

Figure 3: same as Figure 2 but for the 256 observations starting at 38284 s UTC, 11th of March 2004.

For simplicity and because these models apply for the planetary boundary layer, the spectra have not been fitted to dimensionless models for velocity spectra of all three wind components as presented by Højstrup (1981a and 1981b).

Pinus et al. (1966) have computed spectral distributions of turbulence energy in the free atmosphere near jet-stream level from various Russian, Australian and American sources. They found a spread over more than two orders of magnitude of spectral density in the wave length region of CAT, i.e. *L<300* m. This is a somewhat larger variation of turbulent kinetic energy than is indicated by the mesoscale disturbances of *L>10* km. They found partial agreement between subjective pilot's reports and objective gust measurements: from the foregoing it appears that a universally applicable

comparison of subjective pilot reports of CAT with objective turbulence measurements may be made if one allows for psychological reactions by the pilot.

Table 1: Turbulence intensities basically following ICAO (International civil aviation organization) recommendations. Additionally the class extreme is introduced here.

Description	Report	EDR [$m^{2/3}s^{-1}$]	Turbulence intensity class
mdv	mdv	mdv	-1
NIL	L	<0.1	0
LIGHT	ML	0.1-0.2	1
MODERATE	M	0.2-0-4	2
SEVERE	HM	0.4-0.5	3
EXTREM	M	>0.5	4

Dutton (1980) presents the overall results of an extensive turbulence survey organized by the UK Meteorological Office which was carried out during spring of 1976, with the co-operation of the meteorological services and airlines of Austria, Belgium, Denmark, Federal Republic of Germany, France, Republic of Ireland, Italy, Netherlands, Norway, Spain, Sweden, Switzerland and the USA. The pilots of the commercial aircrafts were asked to record the complete turbulence histories during the cruise phase. Table 2 shows the quality controlled subjective pilot reports, in clear air, with the occurrence of turbulence as derived from the MAP and Swiss data in this study.

Table 2: Turbulence intensities following ICAO recommendations from Swiss and MAP airborne observations and pilot report's statistics from an international survey (Dutton, 1980). Note that mdv stays for missing data value.

Description	Dutton	EDR
At least lightly turbulent	9.92%	20.6%
At least moderately turbulent	1.26%	12.7%
Severely turbulent	0.013%	6.47%

Note that the own EDR values in this study were calibrated with one Swiss flight (number 4).

MacCready (1964) proposed an alternative turbulence magnitude scale, with turbulence being much lower for comparable EDR values. With his scale our turbulence intensities might better match the turbulence distribution from Dutton (1980). Still, comprised in the own statistic of Table 2 are included all MAP flights which were trying to fly through turbulent flow, in opposition to the airlines flights which rather avoid it. March 11th 2004 was turbulent in the wider alpine region, which might also explain the rather high proportion of turbulence recordings. Several MAP aircrafts do not cruise higher than the lower half of the troposphere, spending a lot of time in the turbulent boundary layer, so for the P-3, the Arat (see also Figure 8), the Merlin (see also Figure 6), the Metair and the Dornier. Furthermore, Dutton's statistics only apply to clear air, reducing further the count of turbulence encounters.

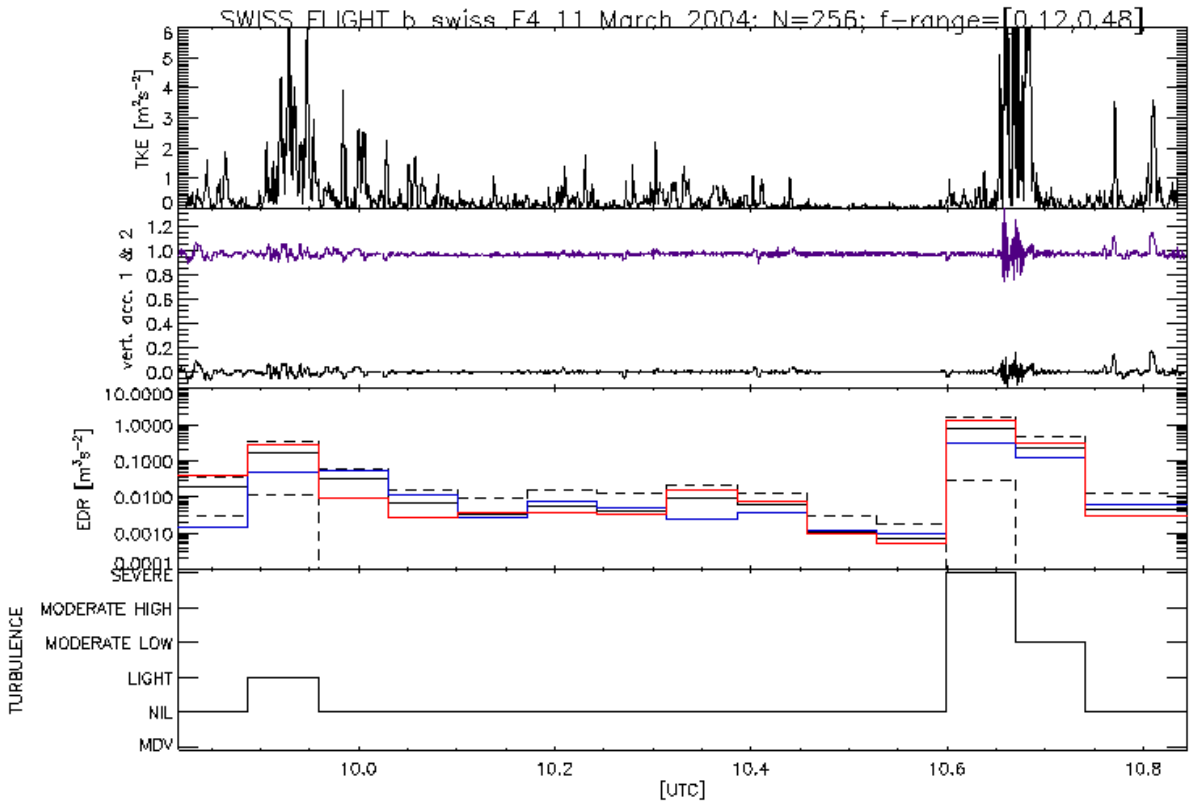

Figure 4 Swiss flight from Rom to Zürich on March 11th 2004. Upper panel shows TKE, computed with running averages of 60 s timespan. The second panel shows the vertical accelerometer as delivered by the flight data recorder. The third panel shows the EDR derived from the zonal (meridional) wind component in blue (red); the mean of both is plotted as the solid black line and +/- a standard deviation as the dotted black lines. The lowermost panel shows the corresponding turbulence intensities as derived following the table 1.

Figure 4 shows the turbulence history during a flight from Rom to Zürich on March 11th 2004 (Swiss flight number 4 of the used data set). The lowermost panel shows the turbulence intensities revealing light turbulence at the beginning of the flight, extreme and moderate turbulence towards the end of the flight. The second lower panel displays the eddy dissipation rate values along the flight. Blue is for the zonal, red for the meridional wind component and black for their mean. The dashed lines show the mean plus/minus one standard deviation. Note that the flight segment shown in Figure 2 and 3 correspond to the 9th and the 12th EDR values respectively.

The two upper panels of Figure 4 show independent measures of turbulence: the turbulent kinetic energy (TKE), defined here as $TKE=1/2(u'^2+v'^2)$, where $u'_i=u_i-\bar{u}$ and $\bar{u}$ denotes the mean wind components, averaged over 60 s. The second panel shows the records of the plane's vertical accelerometers. Note that the root mean square value of aircraft vertical loads, is linearly related to $EDR^{(1/3)}$.

An excellent overall agreement between the 4 panels can be observed: high (low) turbulence intensity is highly correlated with high (low) turbulent kinetic energy and high (low) vertical accelerations of the aircraft. These turbulence intensity cross-validations in Figures 4, 5 and 6 give auspicious confidence in the computation of turbulence classes from *u* and *v* observations as described in this section.

Figure 5 displays the same quantities as Figure 4 for the Falcon MAP flight on November 8 1999. Note that the Falcon vertical accelerometer displayed as a black line is the aircraft's normal (which does not have to be vertical) acceleration as can be seen from the ten high values corresponding to a

narrow turn of the aircraft. For this flight, reasonable agreement between the different turbulence measures is found again.

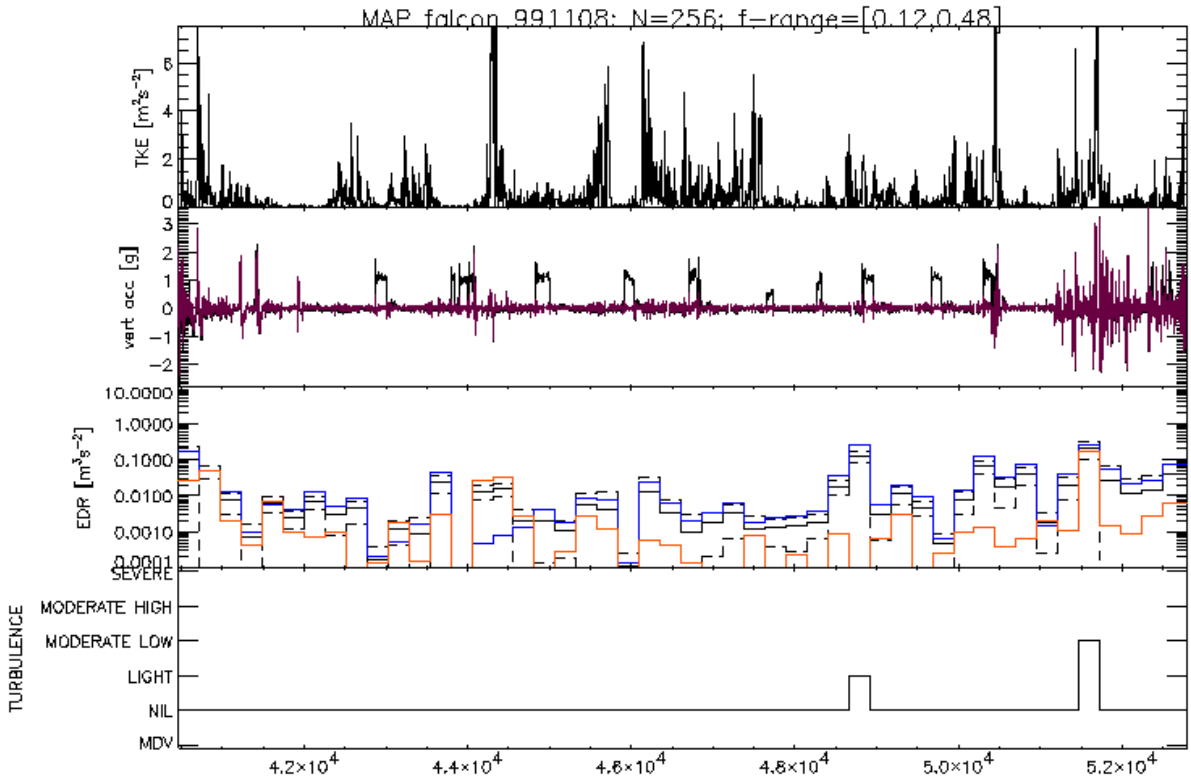

Figure 5: same as Figure 3 but for the falcon MAP flight on 8th November 1999.

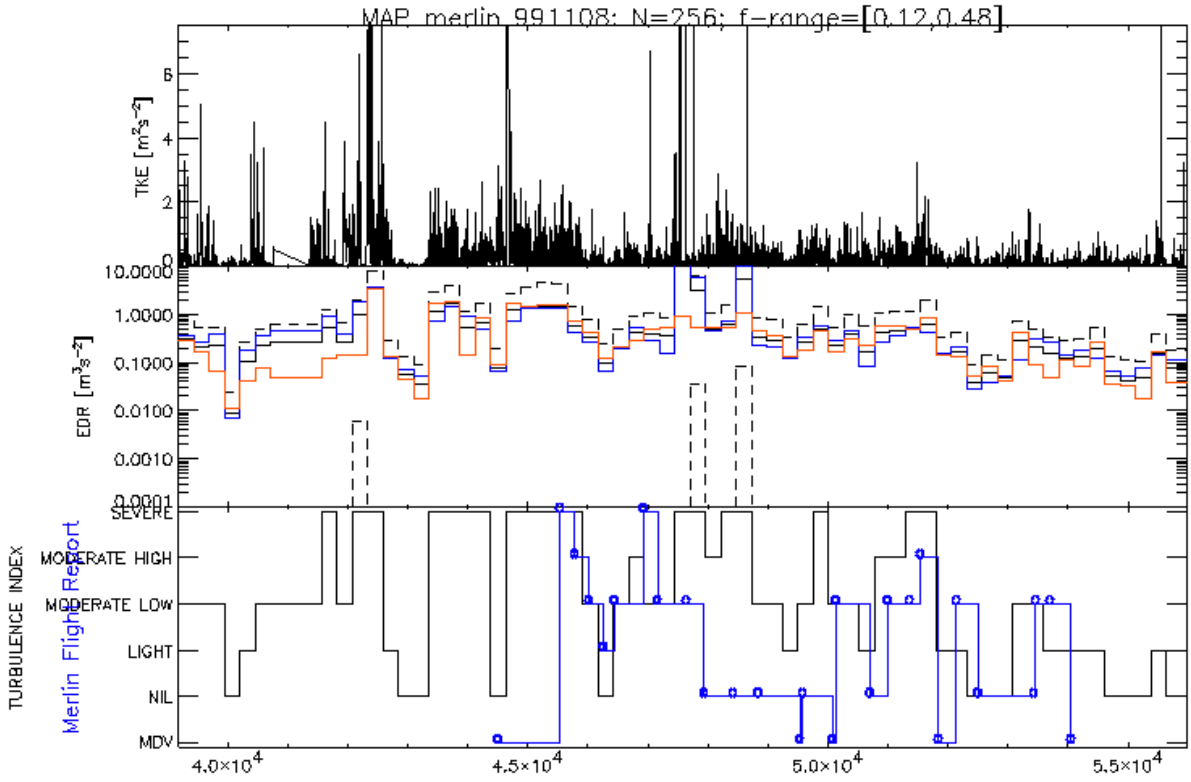

Figure 6: same as Figure 3 but for the Merlin MAP flight on 8th November 1999. This aircraft has no vertical accelerometer but a subjective turbulence report is available, plotted as the blue circles in the lowermost panel.

In Figure 6, a third example of turbulence measures along a flight is shown, namely for the Merlin MAP flight on the same day as the Falcon. Note, that the Merlin cruises at much lower altitudes, between 100 and 600 m over ground with two fast ascends up to 1500 m (not shown), which is an explanation for the higher turbulence intensities encountered. Note that the Merlin is not equipped with vertical accelerometer. However, we have chosen this flight because a subjective turbulence report is available for a portion of the journey, plotted as the blue circles in the lowermost panel of Figure 6. Again the overall agreement is reasonable, even if EDR seems to overestimate the turbulence when compared to the subjective report.

The cross-validation with turbulent kinetic energy and vertical aircraft loads of the results of deriving turbulence intensities from high resolution wind observations, the method of which has been presented in this section, demonstrate that the methodology can be regarded as reliable. Therefore we renounce to the very complex methodology derived as a function of aircraft type by Charman et al. (1995).

4. The mesoscale model aLMo

The aLMo is a fully compressible non-hydrostatic model which is currently operated at MeteoSwiss with a horizontal resolution of 7 km. The number of horizontal grid points is 385 in the (rotated) zonal direction and 325 in the (rotated) meridional direction. The regional model LM is based on the primitive hydro-thermodynamical equations describing compressible non-hydrostatic flow in a moist atmosphere without any scale approximations. A basic state is subtracted from the equations to reduce numerical errors associated with the calculation of the pressure gradient force in case of sloping coordinate surfaces. The basic state represents a time-independent dry atmosphere at rest which is prescribed to be horizontally homogeneous, vertically stratified and in hydrostatic balance.

The basic equations are written in advection form and the continuity equation is replaced by a prognostic equation for the perturbation pressure (i.e. the deviation of pressure from the reference state). The model equations are solved numerically using the traditional finite difference method. The time integration is implicit in the vertical direction and semi-explicit in horizontal directions following the concept of Klemp and Wilhemson (1978). The calculation time step is 40s.

In the operational setting by MeteoSwiss the model has a generalized terrain-following vertical coordinate, which divides the model atmosphere into 45 layers from the earth's surface up to 23600 meters height,. The vertical resolution is highest near the surface with less than 50m vertical grid spacing and increases with altitude. Prognostic model variables are the wind vector, temperature, pressure perturbation, specific humidity, cloud water of grid scale clouds and the fluxes of rain and snow in the latest aLMo version. Turbulent kinetic energy, TKE might be computed in a prognostic or diagnostic way.

The physical parameterization package is completed by a mass flux convection scheme (Tiedtke, 1989), an optional level-2.5 turbulence parameterization, a delta-2-stream radiation transfer scheme, and a 2-layer soil model. Initial and boundary values are provided in this study by the European middle range weather forecasting center (ECMWF) analyses. Additional detailed model description is given by Doms and Schaettler (1999).

5. aLMo wind validation

The “raw resources” for the computation of all turbulence indicators are the horizontal wind components of the aLMo as will be seen in next Section. Therefore, in this Section, we compare the wind observations from the Swiss and MAP data with the model’s wind representation. Figure 7 is a scatter plot of all data pairs with the observed winds on the ordinate and the aLMo winds on the abscissa [m/s]. The black dots are for the zonal wind component and the blue ones for the meridional.

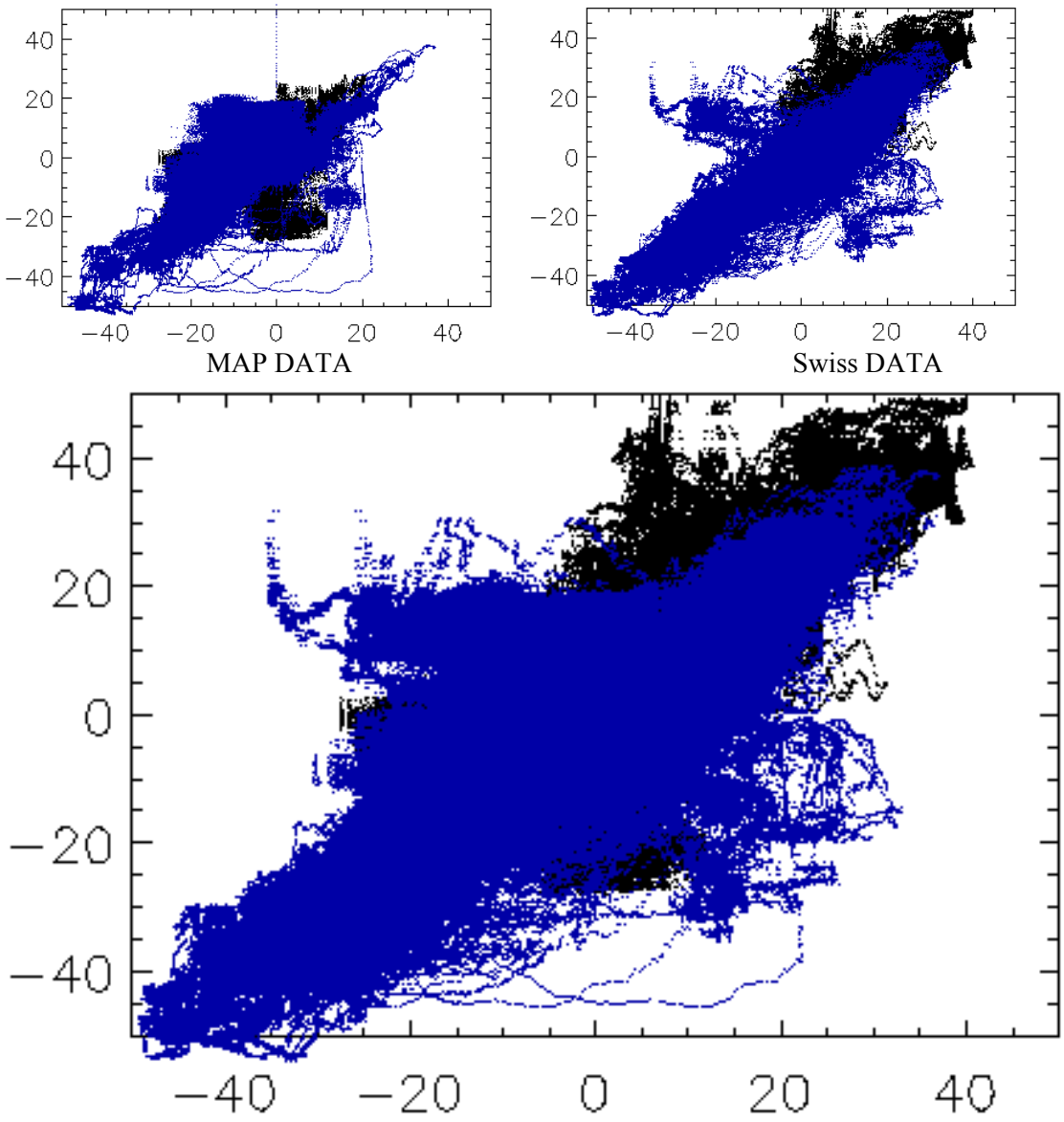

Figure 7: Observed winds on the ordinate [m/s] versus aLMo winds on the abscissa [m/s] for every observation on every considered flight. Black dots are for the zonal wind component and blue ones for the meridional. Upper left panel shows the MAP data, upper right panel shows the Swiss data und the lower panel is the comparison for both data sets.

The mean wind deviations including both data sets leads to wind deviations (model minus observation) of u=2.37 +/- 4.4 and v=-2.22 +/-5.9 m/s, which is more than reasonable for a meteorological model. However, there are single points which denote very large departures from observation, as can be seen from any panel of Figure 7. When looking at both data sets separately, the aLMo model definitively better matches the Swiss data which might be explained by the same reasons as for the discussion of the EDR values, namely that MAP data are generally more turbulent and sometimes in the boundary layer which is not the case of the lower bounded Swiss data.

Figure 8 shows the same data now regrouped in accordance with the forecast time of the aLMo simulation. At least for Swiss and to some extent also for MAP data, the expected effect of a skill dependency to the lead-time of the model forecast cannot be seen with this kind of data. The different output time interval of the aLMo simulation for both data sets, as mentioned in Section 2 can be seen in the upper panels of Figure 8. While MAP data have an almost continuous course along the forecast time (simulations with 1h resolution output), the Swiss data are staggered every three hours, which corresponds to the chosen aLMo output of three hours for these simulations. Although the data was interpolated in the space domain it was not done for the time domain.

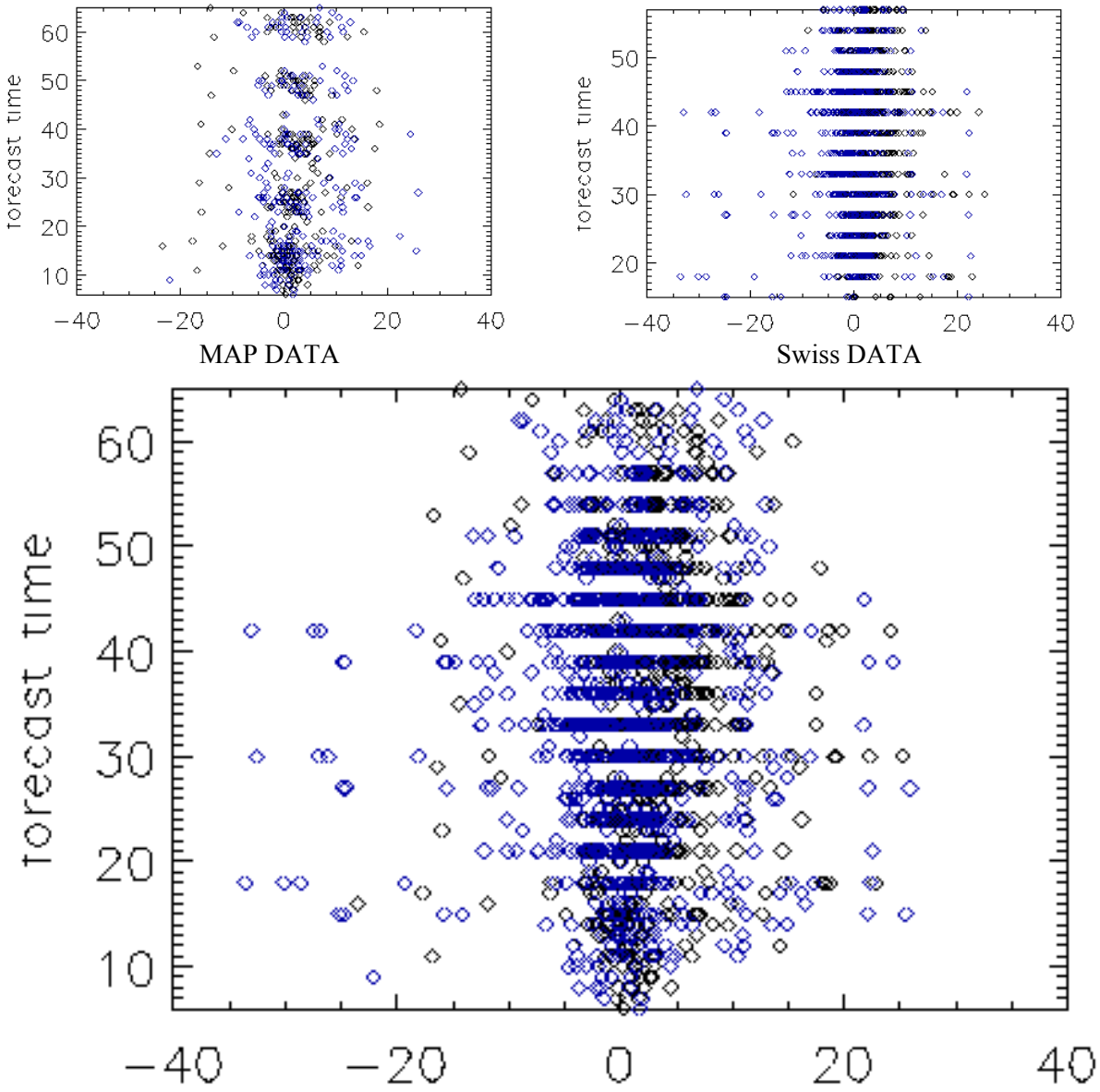

Figure 8: For every aircraft observations of a single flight corresponding to one forecast time [h] of the aLMo model the wind difference has been computed (observation-model), averaged and plotted. Black dots are for the zonal wind component and blue ones for the meridional. The upper left panel show the MAP data, the upper right panel show the Swiss data (note the 3h resolution of the aLMo for this data set) and the lower panel wind errors for both data sets.

Because of this different time resolution of the aLMo simulations for both data sets and as the MAP flights were in average longer than the Swiss flights, there are more circles in Figure 8 for a MAP flight than for Swiss flights. Swiss flights never had more than two corresponding forecast times while MAP flights had up to seven.

6. Turbulence indicators from aLMo

In the following, fourteen different turbulence indicators are introduced. These indicators might be subdivided in two groups, the “fluid dynamical indices” and the “turbulence indices”. The former describes derived fields which are commonly used in fluid mechanics as divergence, deformation, static stability, vertical wind shear and the (Froude) Richardson Number. The latter indices were derived in a specific turbulence forecasting objective as those presented by Ellrod and Knapp (1992),

the one from Colson and Panovsky (1965) and the two indices by Brown (1973). The diagnostic and prognostic turbulent kinetic energy schemes (TKE) used in aLMo are also presented and considered.

In order to illustrate every single indicator, we chose the Swiss flight number 4 in our data set (an Airbus A320-214) with takeoff at the airport of Rome (EBBR) and landing at the airport of Zürich (LSZH) on March 11th 2004. The horizontal sections are all made at 10 km altitude on March 11th 2004 at 12 UTC. The vertical cross sections are four-dimensional linear interpolations (along the flight path, in space and time) of the indicators, which were com**p**uted from aLMo output data.

The synoptic situation on this 11th of March 2004 can be discribed as follows: a deep cyclone is approaching the UK and its center reaches Ireland at about 21 UTC. Over the Po-basin, a weak lee cyclone is growing and deepening as it is advected into south-easterly direction. At around 18 UTC the lee cyclone begins to decay again. A strong upper-level jet, forming a slight ridge over central Europe with insubstantial westwards advection ensures strongly northwestern flow over the Alps during the entire day. The western part of the jet is oriented east-south-east with a wind speed of up to70 m/s on the 300 hPa level.

6.1 Divergence

In horizontal isobaric coordinates, the horizontal divergence of the wind field is defined as:

$$DIV\,\boldsymbol{V} = \nabla \cdot \boldsymbol{V} = \frac{\partial u}{\partial x} + \frac{\partial v}{\partial y} \quad (10)$$

where $\boldsymbol{V}$ is the 2-dimensional horizontal wind vector. Divergence can be described as a relative rate of increase of a material surface. Divergence has two meanings: the mathematical function defined in Equation (10) and the positive values of *div* $\boldsymbol{V}$. This second meaning is the opposite of "convergence", that is of the case when the divergence is negative. In Figure 9, divergence and convergence are separated by the white areas. For the divergence as an indicator, the absolute value of the divergence is taken.

Geostrophic winds are nondivergent; i.e., their divergence is everywhere equal to zero. In other words, the geostrophic motion has no divergence. Divergence charts are therefore very useful to identify regions of strong ageostrophic flows or to identify gravity waves.

Figure 9 shows a horizontal and a vertical cross-section of the aLMo divergence field along with the flight paths of the Swiss flight number 4.The strongest part of the jet could be responsible for the positive negative north-north-west to south-south-east aligned divergence pattern seen on the upper panel of Figure 9. This sequence of divergence bands could be the signature of a jet-instability induced weak gravity wave. Over north-western Iberia, Austria, Corsica and Sardinia signatures of strong geostrophic imbalance might be guessed.

The vertical cross-section of the aLMo divergence field, lower panel in Figure 9, does not reveal any typical gravity wave signature along the Swiss flight, although large divergence and convergence regions are encountered over the Alps. In the following subsection, we take a look at the aLMo representation of vertical propagating gravity waves.

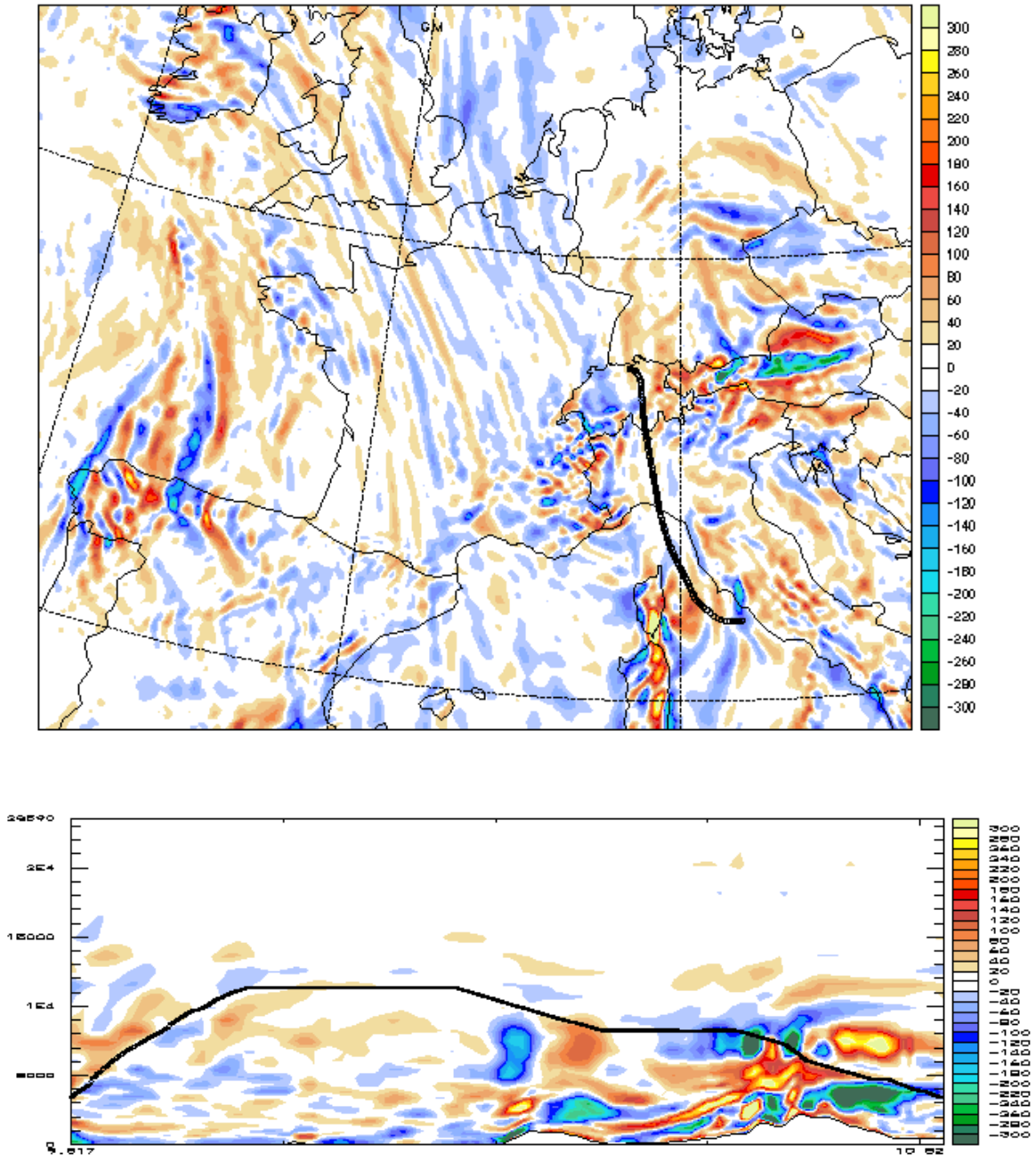

Figure 9: Charts of divergence: the horizontal section in the upper panel is made at 10 km altitude, 11th of March 2004, 12 UTC, and the vertical cross section in the lower panel is a four-dimensional linear interpolation of the divergence from the aLMo data along the flight path of the Swiss flight from Rome to Zürich.

6.2 The upper boundary condition problem

Figure 10 shows examples of four dimensional cross sections along MAP and Swiss flights with gravity waves encounters. In the left column, we show bad examples of vertical propagating GW and in the right panel good representations of vertical propagating gravity waves.

In the left column of Figure 10 it appears that the vertical propagating gravity wave is reflected at the tropopause (upper panel) or at the model top. The reflected wave interacts with the upward propagating wave leading to a vertical aligned spurious divergence pattern.

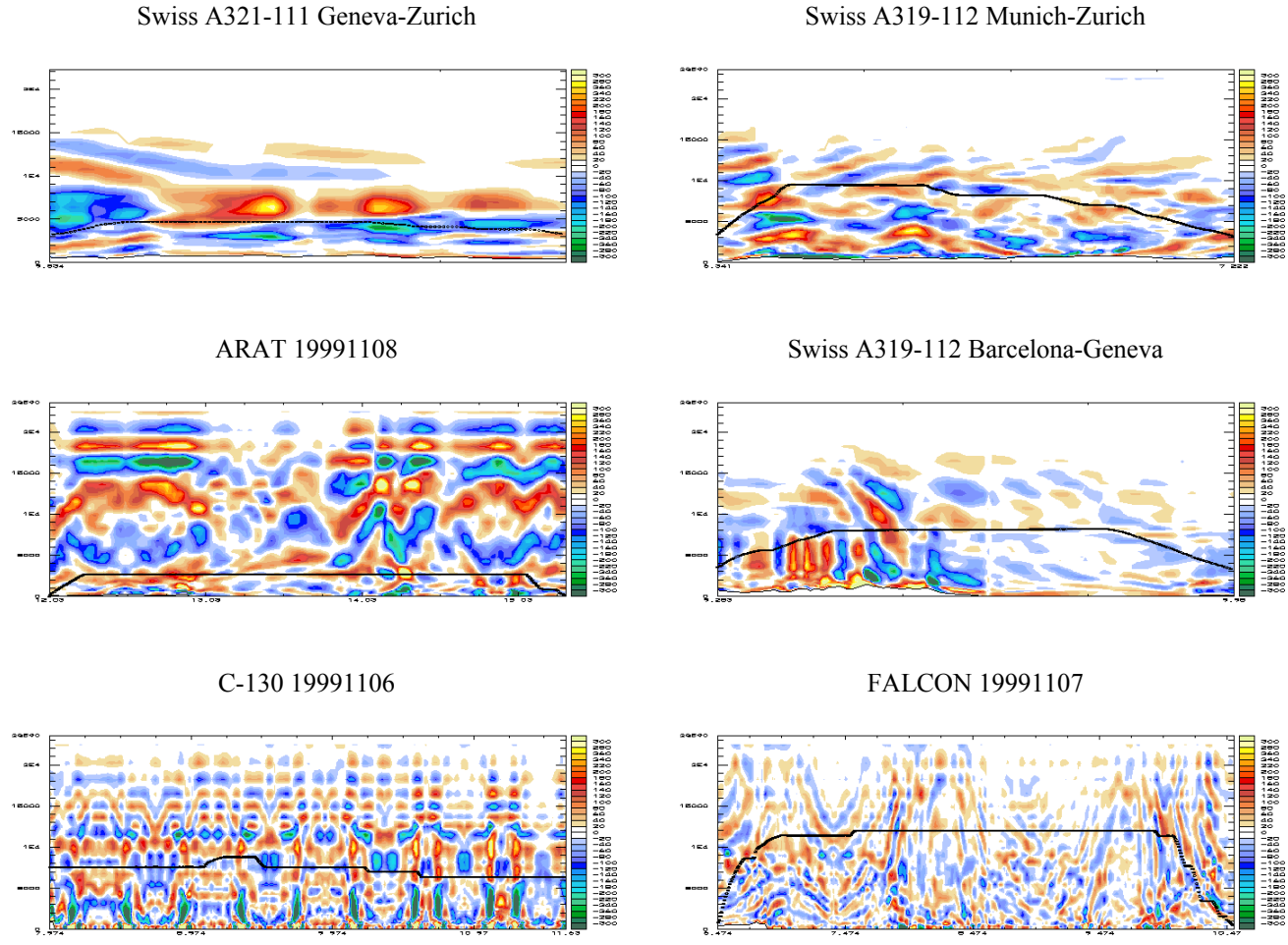

Figure 10: Divergence patterns from aLMo output along selected MAP and Swiss flights.

These standing waves are quasi-stationary as can be seen from the lower left panel, where the C-130 aircraft flies several times the same leg. Vertical propagating GW show a divergence pattern that is back-tilted with respect to the wind direction, as can be seen in the right column of Figure 10. The problem of the upper boundary condition in the aLMo was recognized and newly formulated upper boundary conditions should become operational in July 2005. However, the incorrectly propagating GW should not considerably affect the main meteorological fields of the aLMo.

6.3 Deformation

The deformation, *DEF*, can be divided in stretching deformation, *DST*, and shearing deformation, *DSH*:

$$DEF = (DST^2 + DSH^2)^{1/2} \quad (11)$$

$$DST = \frac{\partial u}{\partial x} - \frac{\partial v}{\partial y}$$

$$DSH = \frac{\partial v}{\partial x} + \frac{\partial u}{\partial y}$$

Efforts to develop a turbulence index (Ellrod, 1989) used the stretching deformation. The *DST* fields related fairly well to observed CAT, but produced excessively large threat areas and were difficult to

interpret due to the presence of both positive and negative maxima. The use of *DEF* eliminated the negative signs, and reduced the contour areas somewhat. Much of the significant CAT, however, seemed to occur in other areas than those of maximum *DEF* alone (Ellrod and Knapp, 1991).

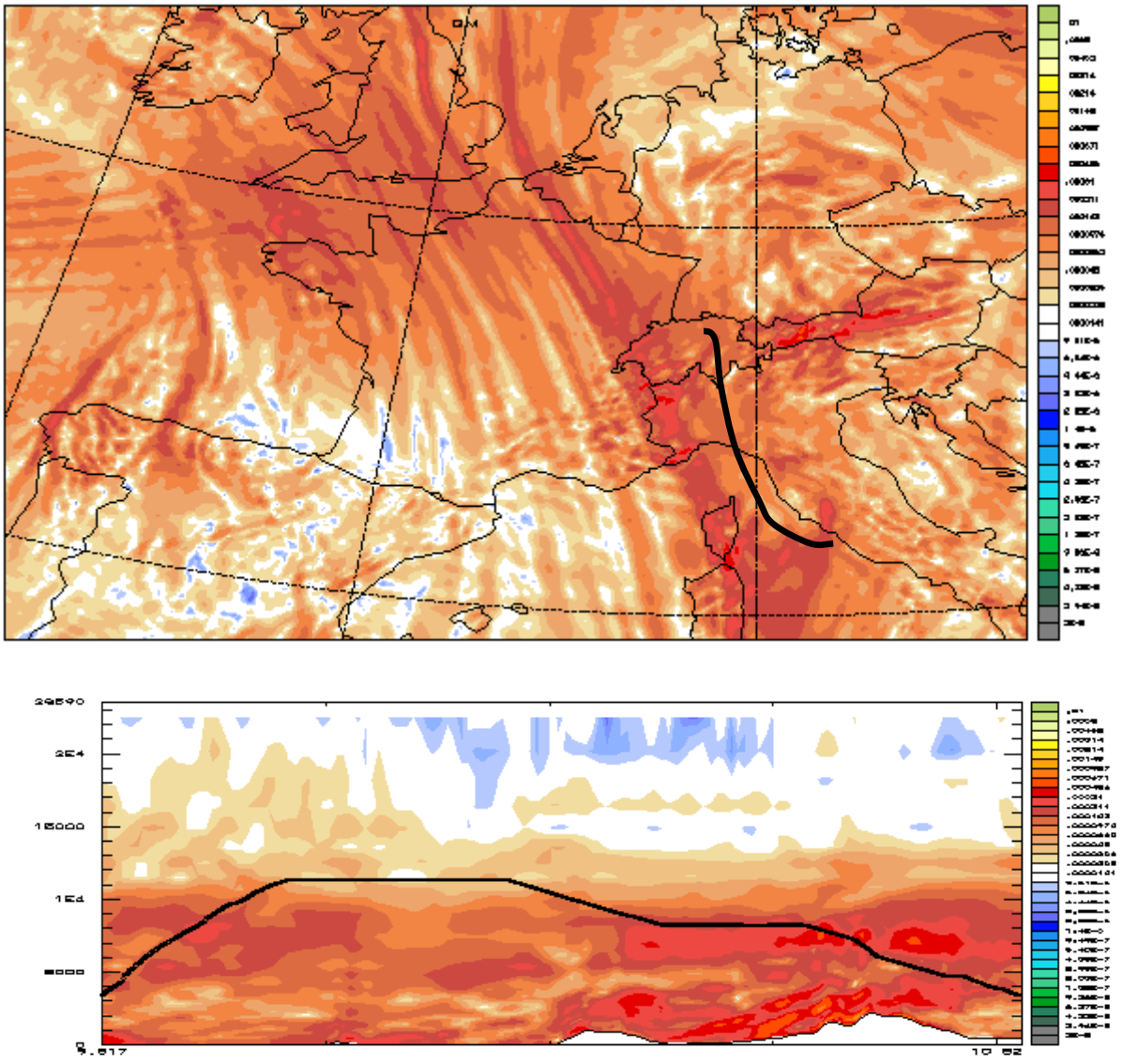

Figure 11: Same as figure 10 but for the deformation aLMo field.

Deformation can be explained geometrically as the rate of change of shape of fluid bodies. This quantity is important in the formation of atmospheric fronts and in the diffusion of materials and properties.

Figure 11 shows two sections in the aLMo deformation fields. Note that *DEF* values are clearly lower in the more stratified stratosphere than in the troposphere. It seems that along its flight, the Swiss aircraft encounters 2 local maxima of *DEF*, which correlate fairly well with the observed EDR (compare also with Figure 4).

6.4 Static stability

Static stability is defined as the stability of the atmosphere in hydrostatic equilibrium with respect to vertical displacements. These displacements are explained by using the parcel method. The parcel does

not allow any transfer of heat with its environment, but allows only adiabatic temperature changes. The stability of the parcel is dependent upon the motion of the parcel after a forced vertical displacement from its original location. As the parcel undergoes adiabatic change, its temperature is compared to that of the surrounding environment so as to relate differences in density. A parcel that returns to its original position is considered stable, while one that will continue away from its original position is unstable. One that is displaced and remains at its new position is considered neutral. The static stability is sometimes referred to as buoyancy, which in atmospheric science has its roots in the so-called Law of Archimedes. The static stability or *NSQ* (squared Brunt Väisälä frequency) is defined as

$$NSQ = \frac{g}{\theta}\frac{\partial \theta}{\partial z} \quad (12)$$

where θ is the potential temperature. A small particle of fluid displaced vertically in a fluid that is otherwise at rest will oscillate about its original position with angular frequency N, called the Brunt-Väisälä frequency.

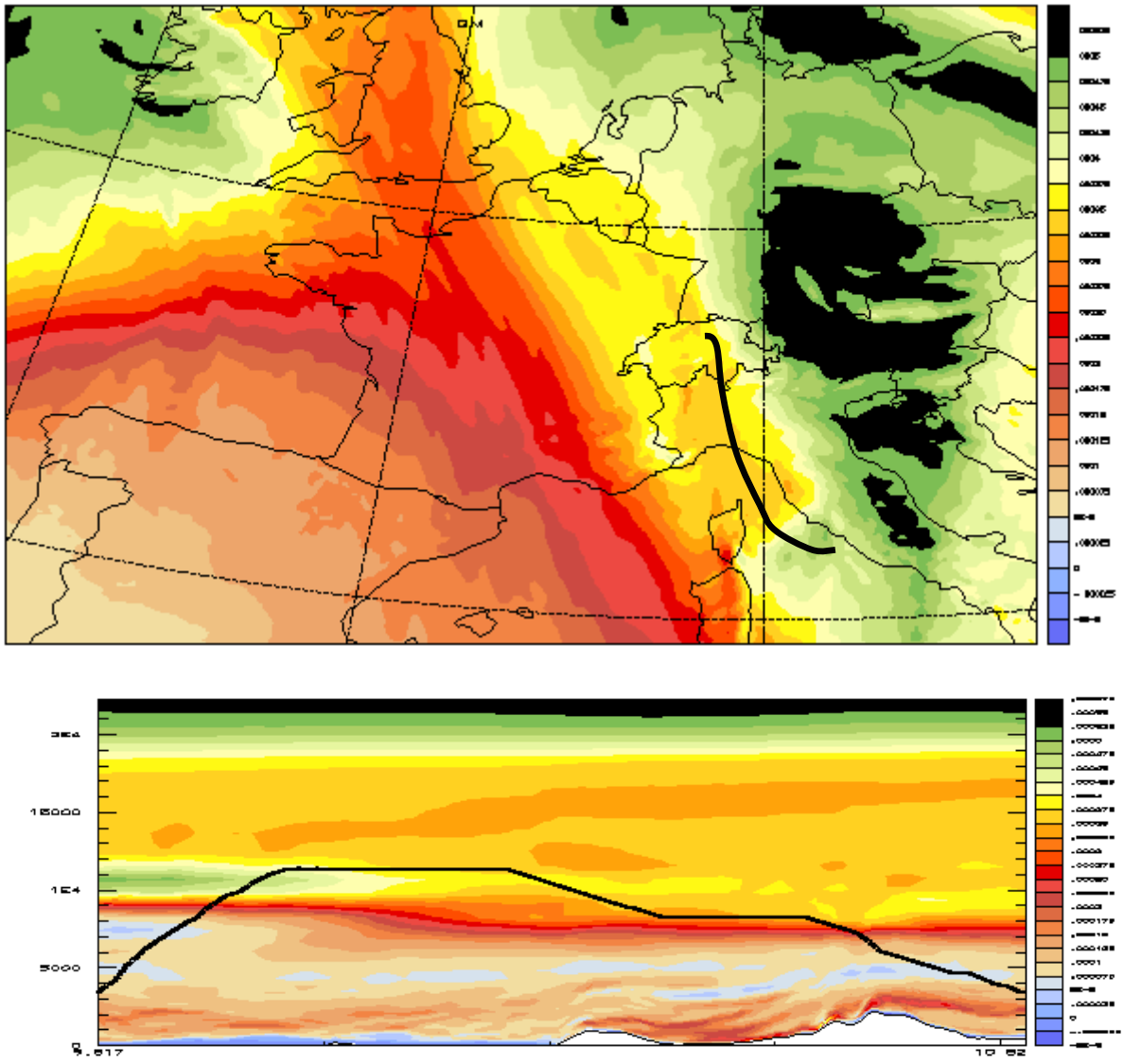

Figure 12: Same as figure 10 but for the static stability aLMo field.

As turbulence is associated with relatively strong vertical motion, it seems obvious to consider NSQ as an indicator. Due to the greater buoyancy, fluid areas with a very low stratification will be much more

likely to get turbulent than areas with a bigger stratification. Figure 12 shows the static stability fields for the Swiss flight from Rom to Zürich. Again, very low Brunt Väisälä frequencies are encountered along the flight, which seem to correlate well with turbulence encounters.

6.5 Vertical Shear

Wind shear is the change in wind speed or direction with height in the atmosphere. Beside NSQ vertical wind shear the most important value leading to small Richardson numbers necessary for KHI. There is always to some extent wind shear observed in the atmosphere. However, large values of wind shear exist near fronts, cyclones, and jet streams. Expressed mathematically, with z as a vertical coordinate, the vertical wind shear is:

$$S_v = \frac{\partial V}{\partial z} \quad (13)$$

Figure 13 shows fields of vertical wind shear. Not surprisingly large values of S_v are encountered in the vicinity of jet streams. Again, two relative maxima at the beginning and at the end of the flight (see lower panel of Figure 13) coincide with the turbulence encounters of the Swiss flight.

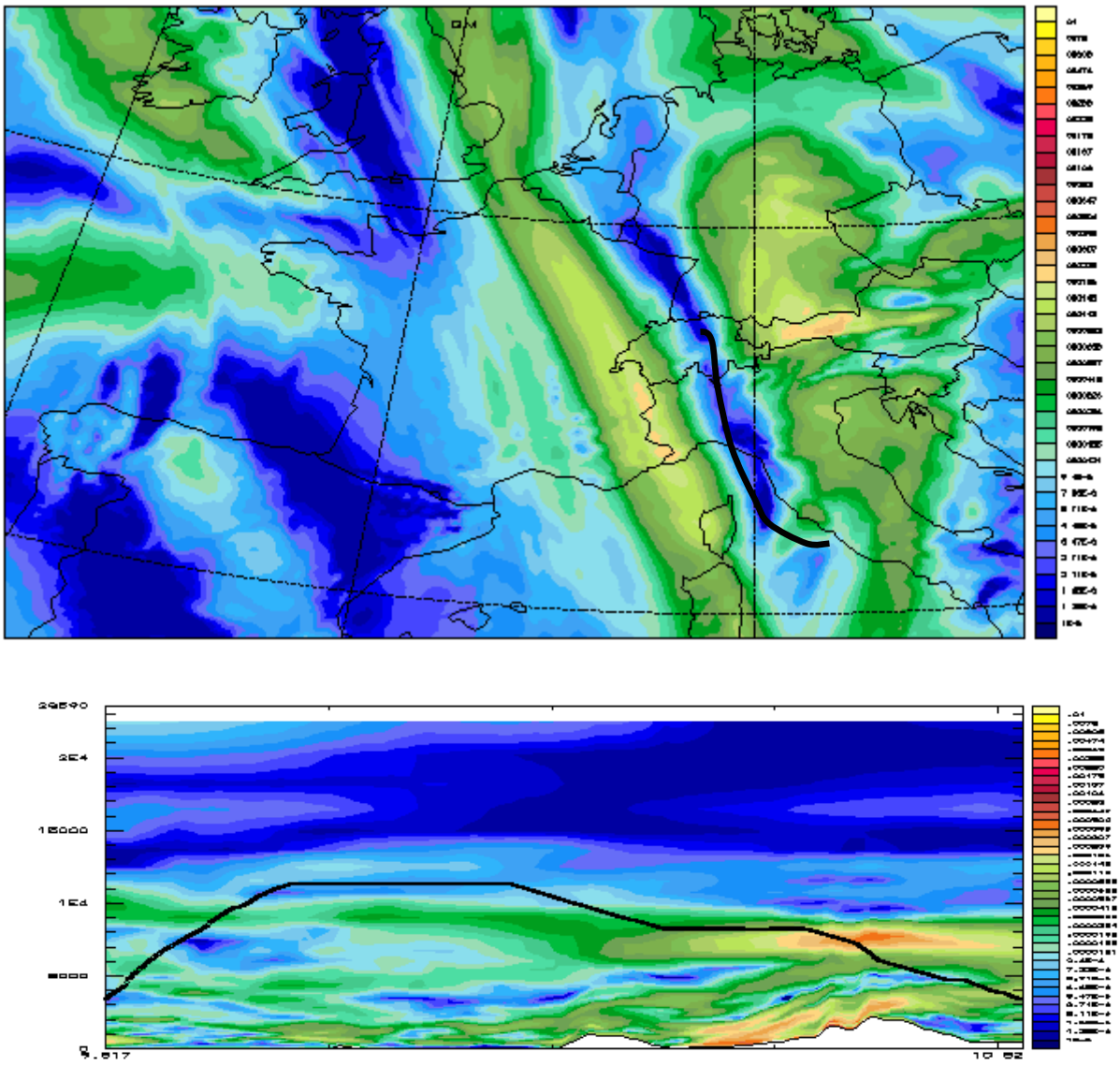

Figure 13: Same as figure 10 but for the vertical shear aLMo field.

6.6 Richardson number and flux Richardson number

The Richardson number or gradient Richardson Number is often defined as the ratio between buoyancy and squared vertical wind shear. Thus, the Richardson number provides a ratio which measures the relative importance of the stabilizing effect of a vertical density gradient and the destabilizing effect of a vertical velocity shear. Here an alternative derivation form is proposed following Colson and Panofsky (1965), starting with the kinetic energy budget equation for steady state, non-advective conditions, and further simplificatinos (14).

$$K_m\left(\frac{\partial V}{\partial z}\right)^2 = K_h \frac{g}{\theta}\frac{\partial \theta}{\partial z} + \varepsilon \quad (14)$$

Turbulent energy is produced at the rate $K_m S_v^2$ where K_m is the kinematic eddy viscosity, which itself depends on the scale and intensity of the turbulence. In a stable environment, this energy production is offset by two factors: the rate of destruction by negative buoyancy, $K_h(g/\theta)(d\theta/dz)$ and the energy dissipation rate, ε. Here K_h is the kinematic diffusion coefficient for heat transfer. Moisture has been neglected. In equilibrium, the maintenance of turbulence requires the Equality 14. Thus, since the dissipation is always positive,

$$Ri \equiv \frac{\frac{g}{\theta}\frac{\partial \theta}{\partial z}}{\left(\frac{\partial V}{\partial z}\right)^2} < \frac{K_m}{K_h} \quad (15)$$

Where Ri is the (gradient) Richardson number. For completeness, let us define the layer Richardson number, Ri_L, as defined by Batchelor (1953) and which is not considered here as a turbulence indicator:

$$Ri_L = RT\frac{\Delta \ln \theta \Delta \ln p}{\Delta V} \quad (16)$$

where $\Delta\theta$ and ΔV are the potential temperature and wind velocity changes across a layer Δz of mass $\Delta p/g$ per unit area.

Dynamic meteorology and observations show that a stably stratified fluid flow will become hydrodynamically unstable and break into a disorderly, turbulent mode when the Richardson number is smaller than a critical Richardson number, Ri_c. In literature there are different values for the critical Richardson number (Ri_c): Djurić (1994) proposed Ri_c=0.21, Wanta (1953) quoted for curved wind profiles Ri_c=0.04, Lyons et al. (1964) find that, near the ground, noticeable turbulence disappears for Ri>0.5. Taylor (1931) concluded from perturbation theory the critical Richardson number to be 0.25 which is a commonly accepted value for Ri_c,. A serious difficulty in settling on a definite value of a critical Richardson number is that the observed Richardson number in a given situation depends on the resolution of the observations. Of course this holds also for gridded data.

Figure 14 shows this Richardson number field, computed with the aLMo hindcast. Note that the numerical distribution of Ri is very broad: from negative values up to several thousands. Note also the unsurprising strong anticorrelation between the Richardson number field and the vertical wind shear (Figure 13). The layer with high vertical wind shear or low Richardson number (see Figure 14 lower panel) corresponds well to the high turbulence intensities from the Swiss flight observations.

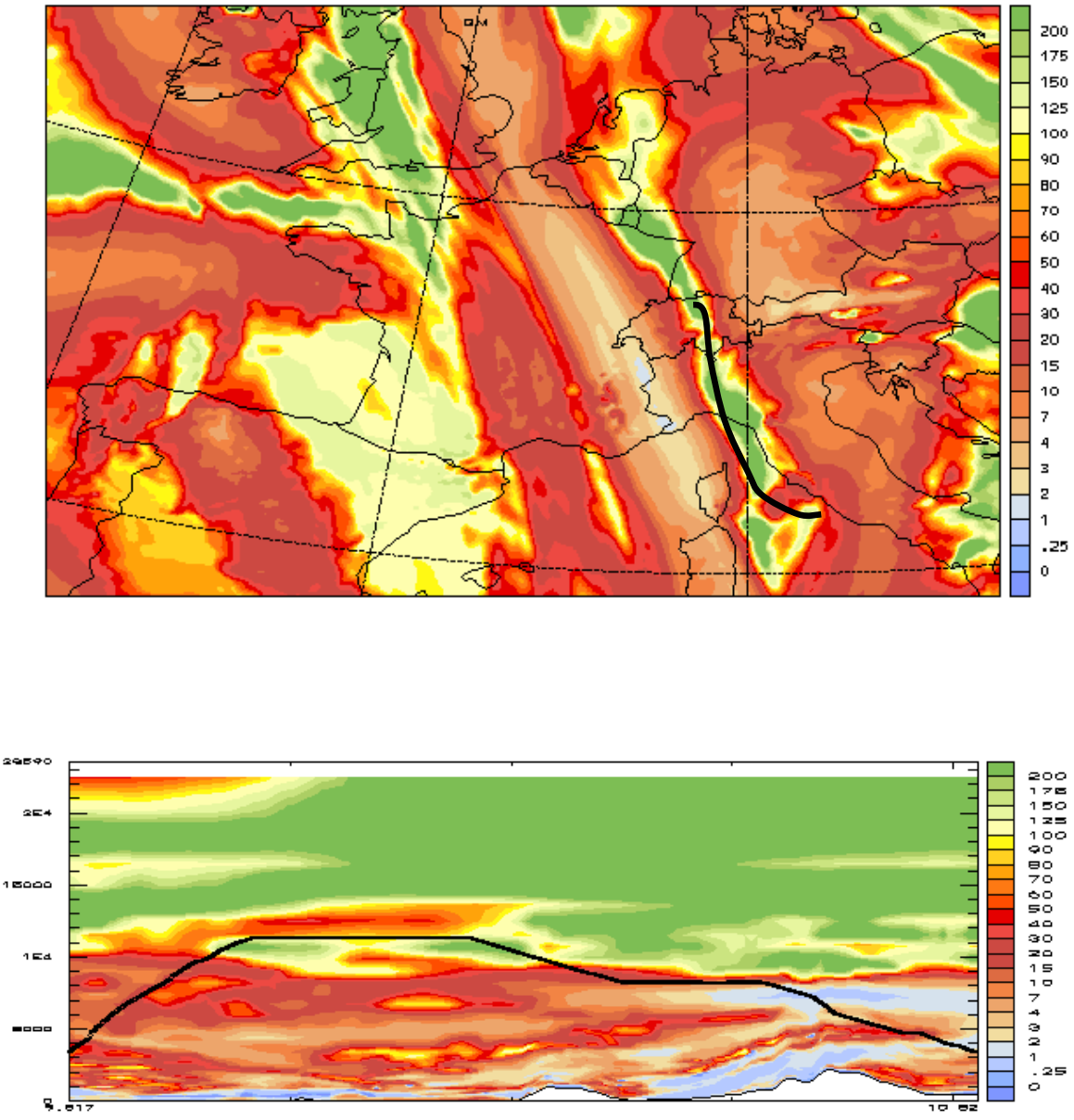

Figure 14: Same as figure 10 but for the aLMo Richardson number field.

The flux Richardson number is a dimensionless number which is defined from the TKE-equation and that can, in the limit of K-theory, be written as the ratio of the vertical heat flux and the vertical flux of momentum. *FRi* is calculated in the aLMo diagnostic from the quadratic equation:

$$FRi = c_1 \cdot (Ri + c_2 - \sqrt{Ri^2 - c_3 \cdot Ri + c_2^2}) \quad (17)$$

The constants c_1, c_2 and c_3 in the relation for the flux-Richardson number are derived from universal constants of turbulence theory and from matching conditions to surface layer scaling. They take different values for stable conditions ($Ri>0$) and for unstable conditions including the neutral case ($Ri \leq 0$). The values for these constants are given in Table 3.

Table 3: Numerical parameters for the computation of the Flux Richardson number (Equation 17) as parameterized in the aLMo mesoscale model.

	stable	unstable
c_1	0.8333	1.285
c_2	0.2805	0.2305
c_3	0.1122	-0.1023

The flux Richardson number (see Figure 15) has a numerical distribution which is much narrower than the Richardson number. However, both patterns of the the distribution in the vertical cross section of the Swiss flight look quite similar.

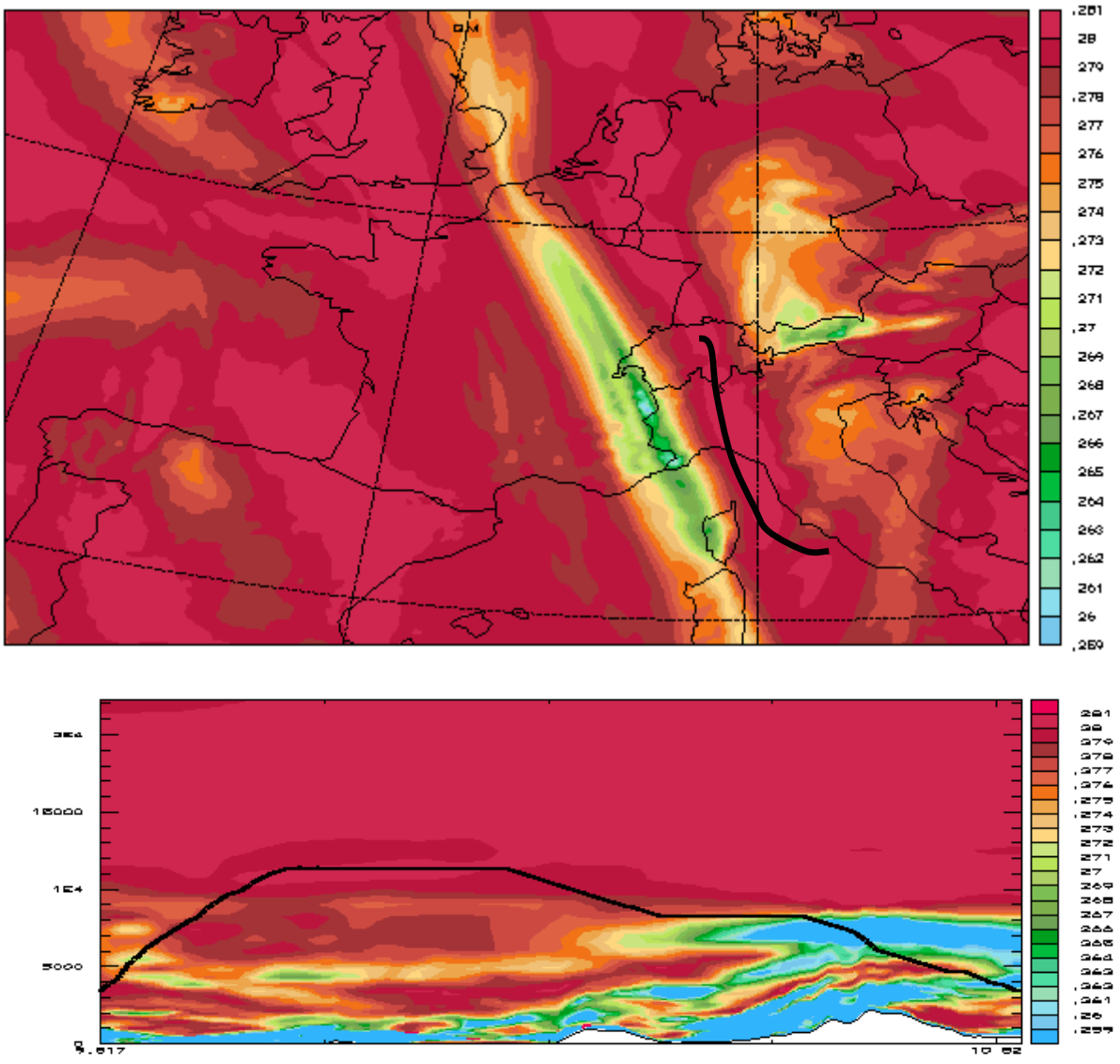

Figure 15: Same as figure 10 but for the aLMo flux Richardson number field.

6.7 Ellrod and Knapp indicators

The paper by Ellrod and Knapp (1992) describes two objective forecast indices based on horizontal deformation, vertical wind shear and divergence. The horizontal temperature gradient is related to vertical wind shear by the thermal wind relationship. Therefore, frontogenesis will result in an increase in vertical wind shear, and an increase in the likelihood of CAT occurrence. Mancuso and Endlich (1966) correlated frequency of moderate or severe turbulence to numerous meteorological parameters

thought to be significant in CAT generation. The product of S_v and *DEF* resulted in the highest correlation (0.43-0.48), which was about double the value for S_v alone. Dutton (1980) found a poor correlation between *DEF* and CAT, but did not consider the product of *DEF* and S_v. Thus the first Ellrod and Knapp indicator, EL1, is simply:

$$EL1 = Sv \times DEF \quad (18)$$

and Figure 16 shows two sections of this turbulence indicator. Not astonishingly, the map resembles or has aspects of both, the S_v field (Figure 11) and of the *DEF* field (Figure 13).

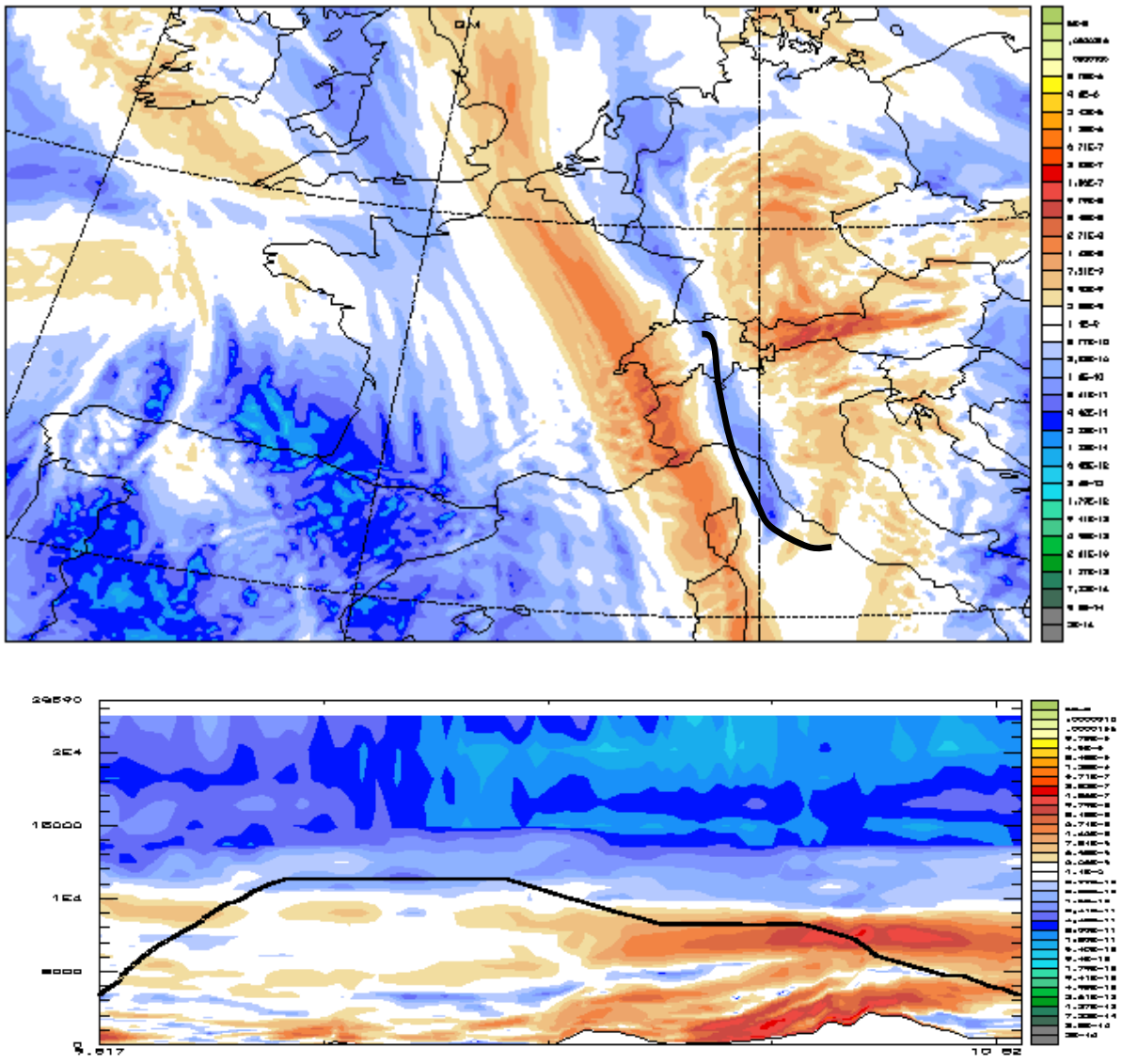

Figure 16: Same as figure 10 but for the aLMo Ellrod and Knapp 1 indicator.

The second indicator, EL2, takes further account of the convergence (negative of divergence), because in some cases, it still contributed significantly to CAT potential (Kao and Sizoo, 1966):

$$EL2 = Sv \times \left(DEF - DIV\right) \quad (19)$$

All terms comprising the Ellrod and Knapp parameters are kinematic, and thus describe atmospheric flow conditions without regard to pressure forces. Figure 17 shows maps of *EL2*. When comparing with the EL1, it appears that the divergence term has a marked influence, at least what the horizontal section is concerned.

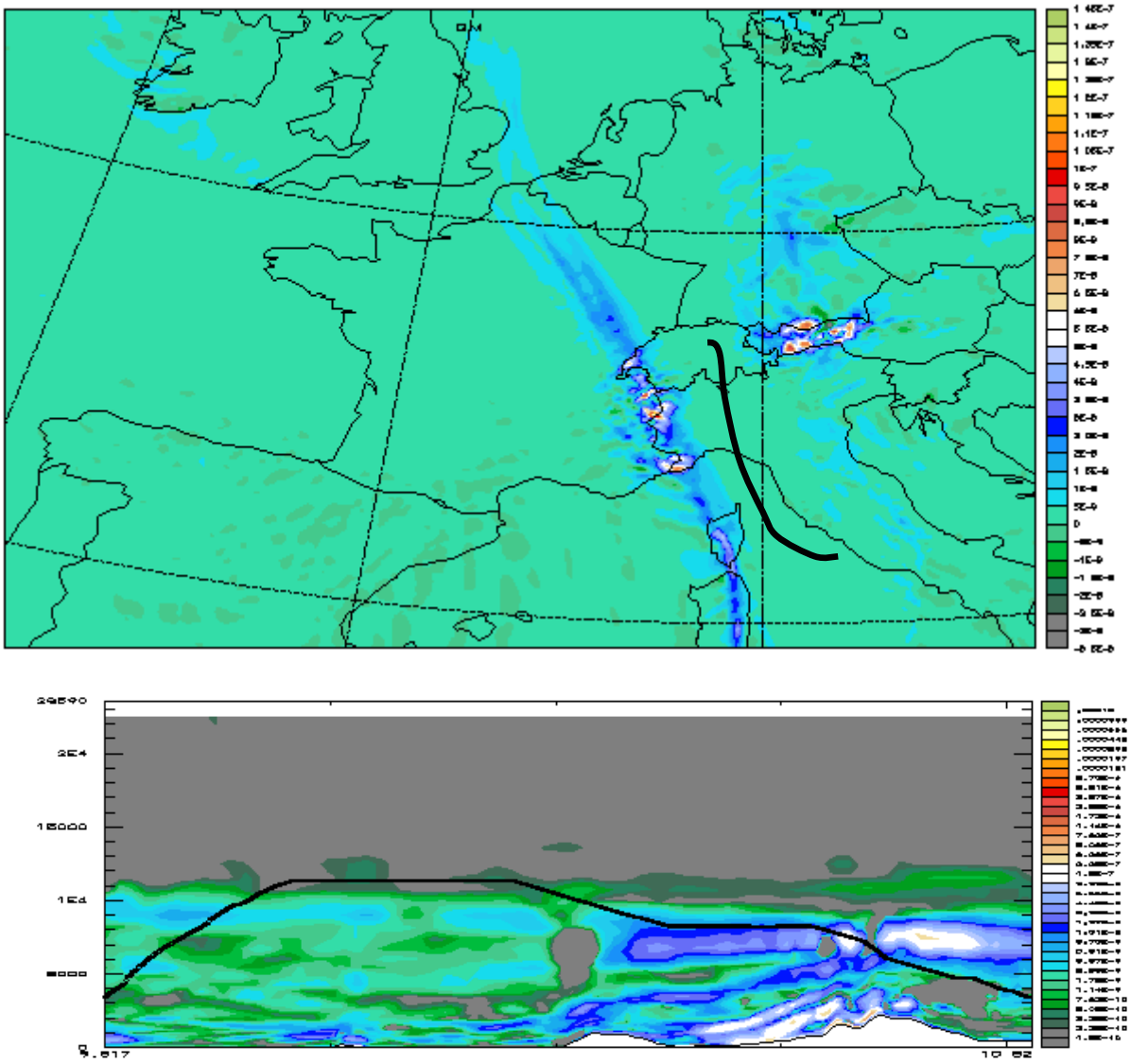

Figure 17: Same as figure 10 but for the aLMo Ellrod and Knapp 2 indicator.

6.8 Colson and Panofsky indicator

The index proposed by Colson and Panofsky (1965), *COP*, is defined as follows:

$$COP = Sv^2\left(1 - \frac{Ri}{Ri_{crit}}\right) \quad (20)$$

COP should be a quantity proportional to the intensity of the turbulence. The discussion earlier suggests that there is no agreement about a numerical value of Ri_{crit}. For this *COP* index we have chosen:

$$Ri_{crit} = \frac{1}{\alpha}\frac{K_m}{K_h} \hat{=} 0.75 \quad (21)$$

Note that this index might not be as robust as other ones as Ri_{crit} is a free parameter which may be set arbitrarily. In the present study Ri_{crit} was not adjusted and the recommended value was used

throughout. The wind difference, S_v, which should be measured vertically across the front, can perhaps be determined almost equally well over a vertical distance of 1000 ft or more, since if the front exists in such a layer, most of the wind difference is due to the change of wind through the narrow frontal zone (Colson and Panofsky, 1965). Of course, in the present study, *COP* was computed for every grid point of the aLMo model and the vertical wind shear was computed with centered finite differences on the model levels. Figure 18 shows examples of *COP* fields.

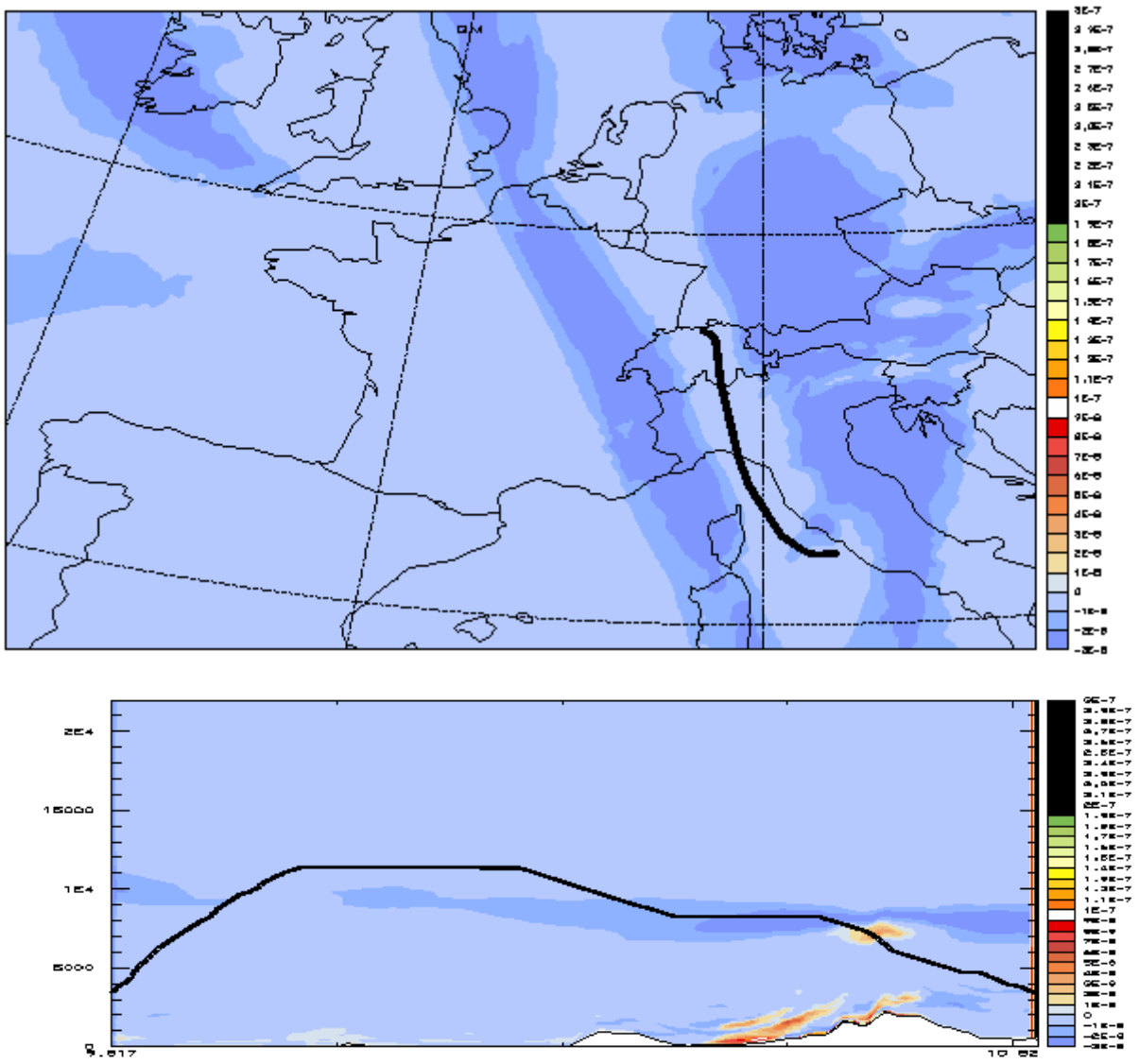

Figure 18: Same as figure 10 but for the aLMo Colson and Panofsky indicator.

6.9 Brown indicators

Brown (1973) proposes a modified Richardson tendency (see below) as a first index, *BRO*:

$$BRO = \sqrt{0.3 \cdot \zeta_a^2 + DSH^2 + DST^2} \quad (22)$$

where ζ_a^2 is the vertical component of absolute vorticity. The *BRO* index, computed with aLMo data is illustrated in Figure 19, for the same Swiss flight. Not astonishingly, the field shows the same main features as the *DEF* field in Figure 11. Again a subjective correspondence with the EDR values along the flight shown in Figure 4 is found.

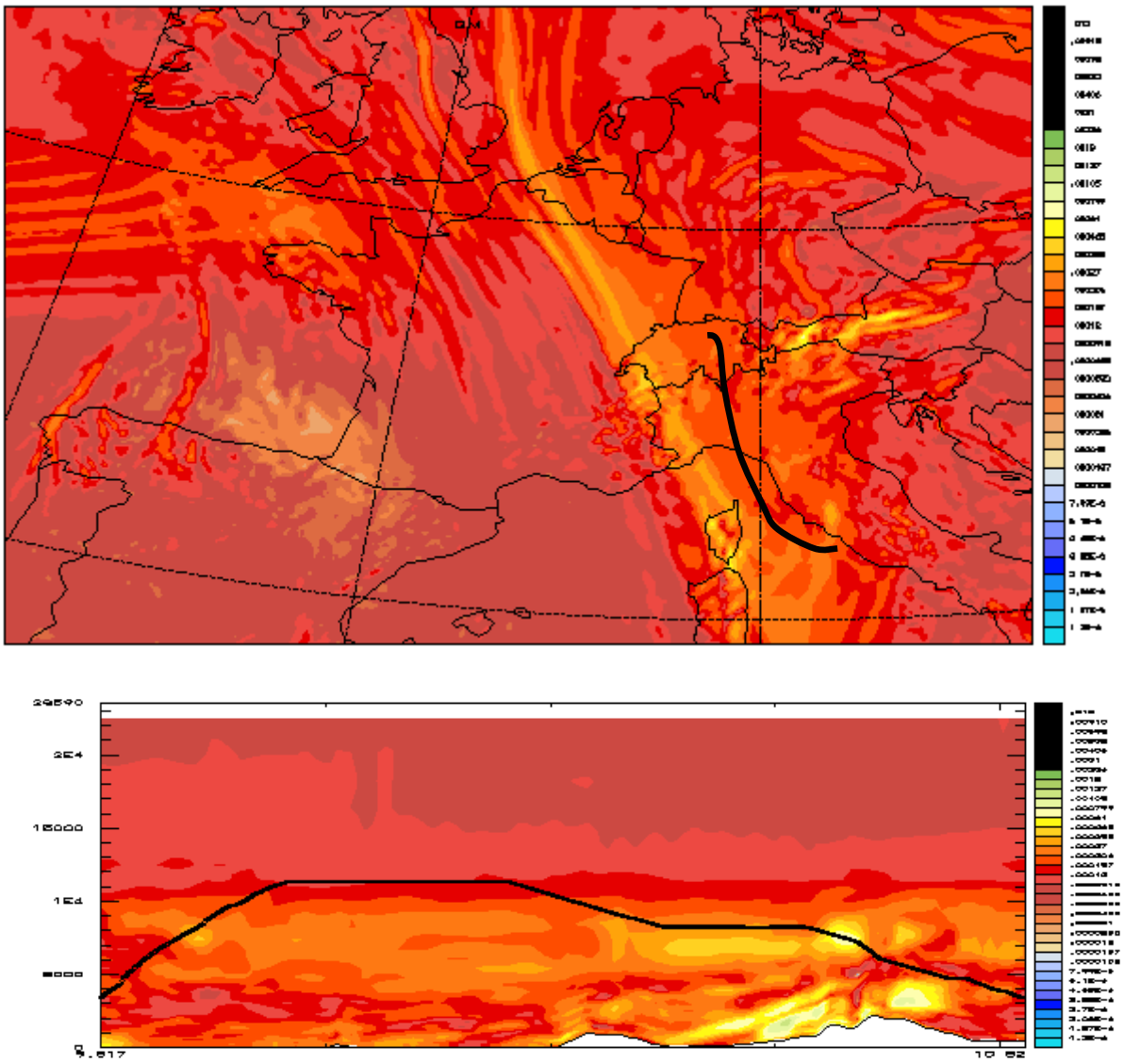

Figure 19: Same as figure 10 but for the aLMo Brown indicator.

Roach (1970) postulated that if the synoptic-scale deformation processes reduce *Ri* across a layer below its critical value the resultant turbulence tends to increase *Ri* in this layer. The turbulence will decay unless *Ri* can be maintained below a critical value by the deformation processes. An expression for the energy dissipation ε was derived by assuming that the turbulence (increasing *Ri* across the layer) works against the deformation processes (reducing *Ri* across the layer), the net result being that *Ri* across the layer is held to a small limiting value. The resulting expression, *EDB*, as modified by Brown is:

$$EDB = \frac{\mathrm{D}Ri}{\mathrm{D}t}\frac{Sv^2}{24} \approx BRO\frac{Sv^2}{24} \quad (23)$$

A difficulty arises in evaluating *EDB* synoptically because CAT is usually distributed as an ensemble of patches of various thicknesses throughout a region of the atmosphere of synoptic dimensions.

Figure 20 displays the fields of the modified Eddy dissipation rate, *EDB*.

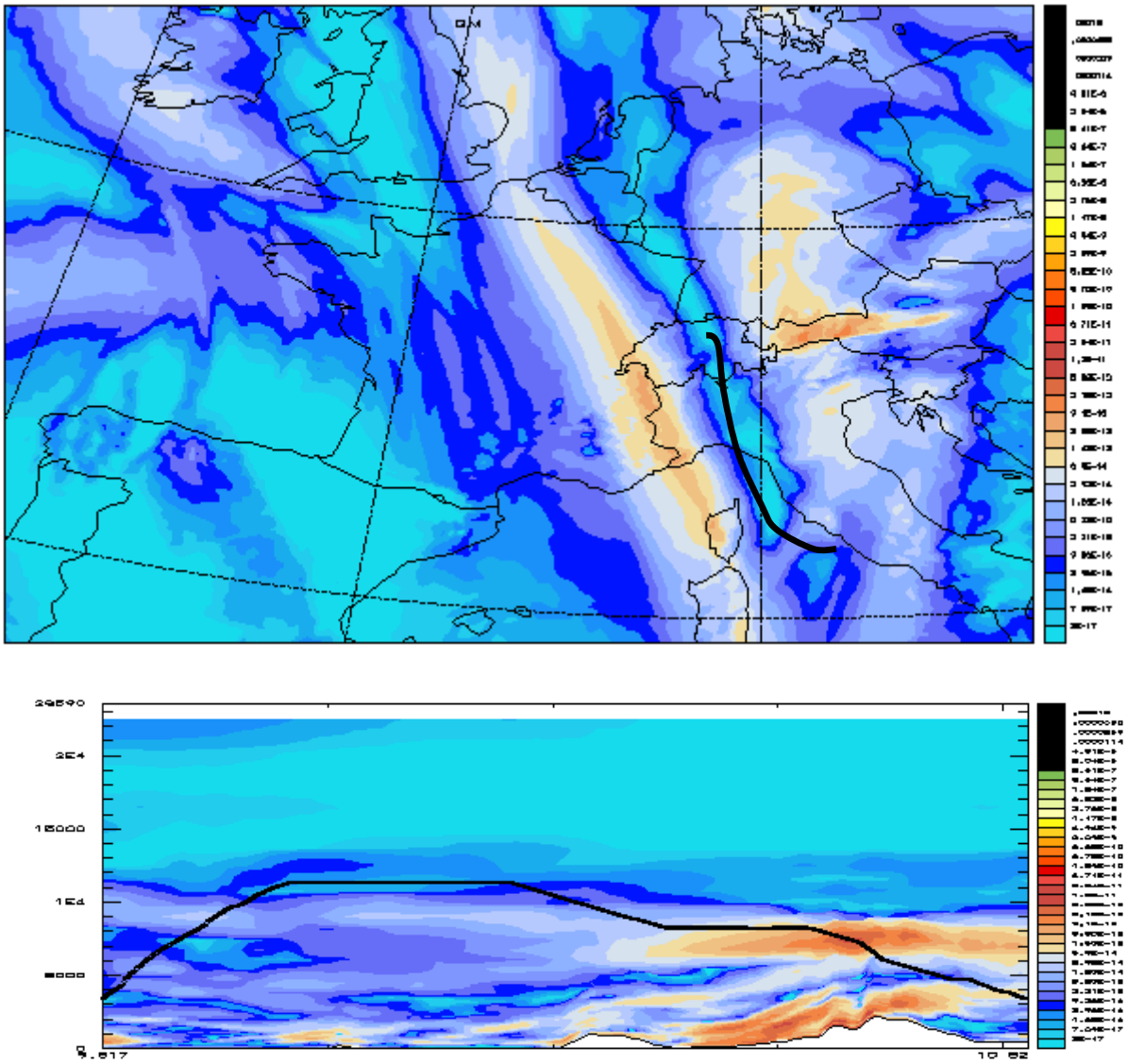

Figure 20: Same as figure 10 but for the aLMo Brown EDR indicator.

6.10 Diagnostic Turbulent energy indicators

The parametrization of small-scale turbulence links the resolvable scales and the nonresolvable fluctuating scales of motion. An offline turbulent scheme is available, taken from the aLMo source code (Doms and Schaettler, 1999) which allows ulterior diagnosing of the turbulent energy, TKE_D,

$$TKE_D = 0 \quad if\ Ri \geq 0.38$$
$$TKE_D = c_z \cdot l \cdot \left(K_M S_V^2 - K_H N^2\right) \quad if\ Ri < 0.38 \quad (24)$$

where c_z is a numerical parameter given in table 4, K_M and K_H are the 3D kinematic eddy viscosity coefficients for momentum and heat transfer. Here again the discordance upon the numerical value of Ri_{crit} is illustrated. This Ri_{crit}=0.38 was adopted from the code even though it does not correspond to the other values of Ri_{crit} chosen in this study (see Section 6.8).

Figure 21 illustrates that that this parametrization is essentially thought for the turbulent fluxes to provide an exchange of momentum, heat and humidity between the earth's surface and the overlying planetary boundary layer. TKE_D is therefore of crucial importance for a successful numerical

simulation of atmospheric flow but (mostly) useless for turbulence indication in the free atmosphere. Namely on the upper layers the value is mostly zero.

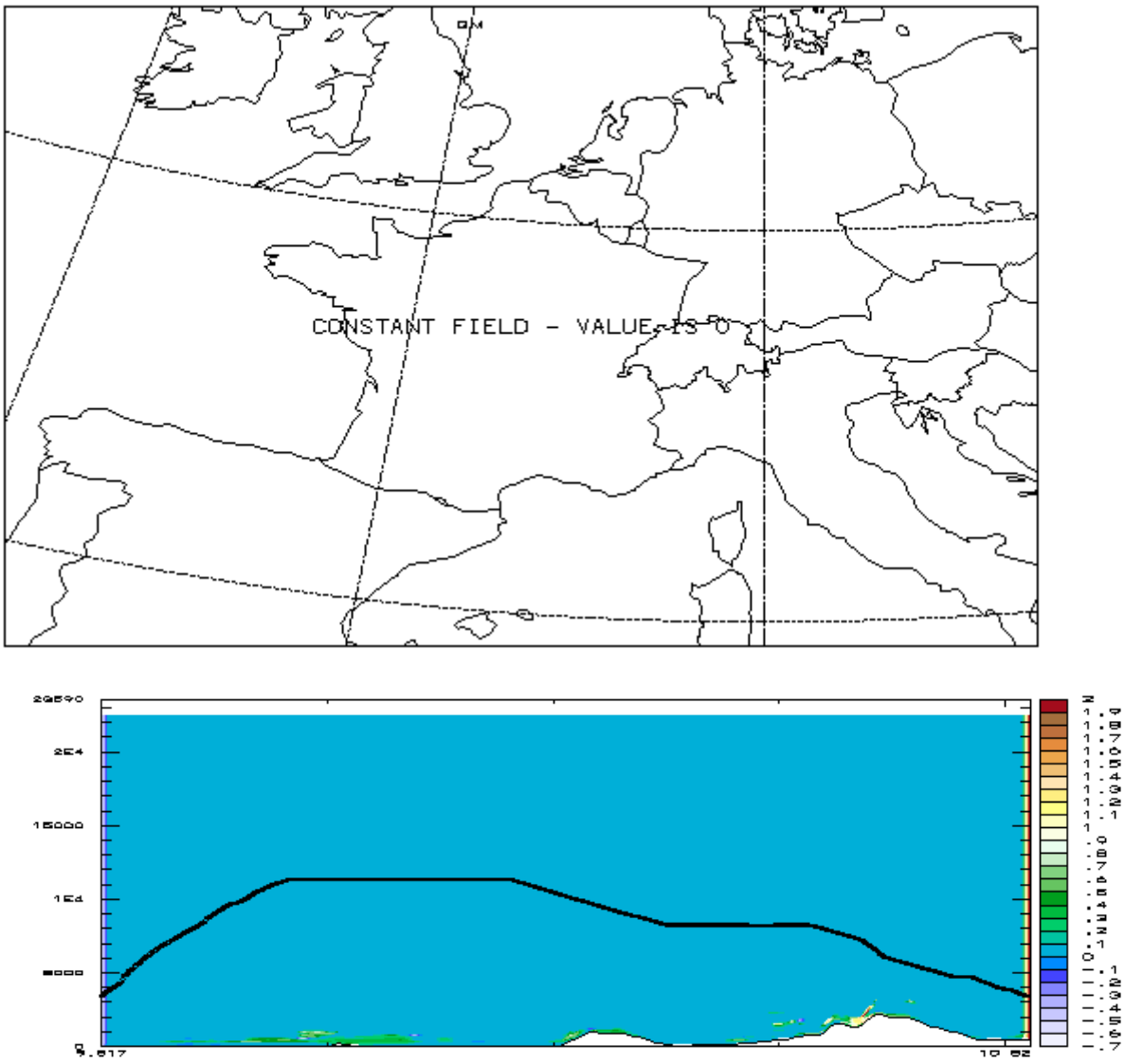

Figure 21: Same as figure 10 but for the aLMo diagnostic turbulent kinetic energy, TKE_D.

Therefore the parameter was not considered for the ranking of the indicators when considering Swiss data. For some MAP flights the parameter did provide indeed values that were reasonable and different from zero, but mainly at very low altitudes.

For TKV, the 3D kinematic eddy viscosity coefficient for momentum transfer, K_M had to be computed. This additional indicator is parameterized as follows:

$$TKV \equiv K_M = l^2 S_m^{3/2} \sqrt{S_V^2 - \alpha_n S_h N^2} \quad (25)$$

The characteristic length scale l for vertical mixing is calculated according to:

$$l = \frac{\kappa z}{1 + (\kappa z)/l_\infty} \quad (26)$$

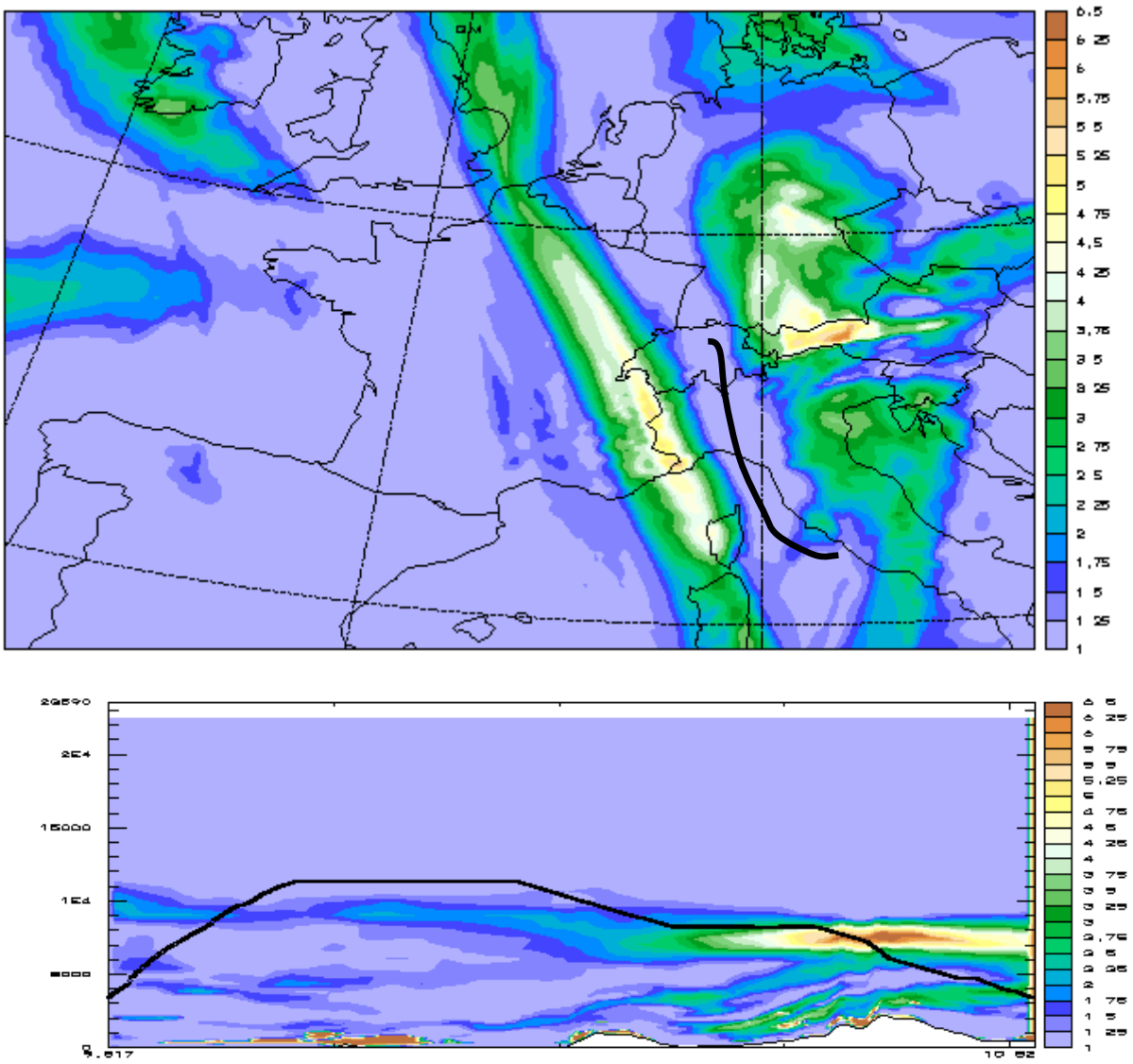

Figure 22: Same as figure 10 but for the aLMo diagnostic turbulent kinetic energy, TKV.

where κ is the von-Karman constant and l_∞ is an asymptotic mixing length. The constant parameter α_n denotes the ratio of the diffusion coefficients for heat and momentum at neutral thermal stratification. S_m and S_h are stability functions which read

$$S_h = \frac{1 - b_1 \Gamma}{1 - b_2 \Gamma}$$

$$S_m = 1 - \frac{\alpha_0}{S_h} \quad (27)$$

thus depending on the stability parameter Γ, defined as

$$\Gamma = \frac{FRi}{1 - FRi} \quad (28)$$

FRi denoting again the flux-Richardson number (see Equation 17). The numerical values of b_1, b_2, α_0 are given in Table 4.

Table 4: Numerical parameters for the computation of TKE_D, S_h and S_m(Equations 24 and 27) in order to calculate the coefficient for vertical turbulent transport of momentum, *TKV* (Equation 25).

	Stable	Unstable
α_0	3.7	4.025
b_1	2.5648	3.337
b_2	1.1388	0.688
c_z	16.6	16.6

6.11 Prognostic turbulent kinetic energy

Within COSMO it is the aim to have as far as possible a unique source code for all model instances used within the consortium. Therefore, the new turbulence parameterization (Raschendorfer, 2003 and Herzog et al., 2001) was built in a fairly general parameterization scheme for all subgrid-scale flow patterns. To this end, the turbulence scheme contains some considerable generalizations. A prognostic level 2.5 closure scheme was therefore chosen for the prognostic TKE-equation.

The new scheme includes the transition of turbulence which contributes mainly to the fluxes (diffusive turbulence) to very small scale (dissipative) turbulence by the action of very small scale roughness elements, and the handling of non-local vertical diffusion due to boundary layer scale turbulent motions. Most important seems to be the introduction of a parameterization of the pressure transport term in the TKE-equation that accounts for the TKE-production by subgrid-scale thermal circulations. The whole scheme is formulated in conservative thermodynamic variables (with the respect to moist adiabatic processes) together with a statistical cloud scheme in order to consider subgrid-scale condensations effects.

The present approach specifies the turbulence coefficients after Prandtl and Kolgomorov :

$$K_m = \Phi_M \Lambda \sqrt{TKE} \quad (29)$$

$$K_h = \Phi_H \Lambda \sqrt{TKE} \quad (30)$$

Apart from having still undetermined factors Φ_m and Φ_h as functions of stability and turbulence length scale Λ, the $K_{m,h}$ – specification needs the information of turbulent kinetic energy. Thus, the diagnostic TKE-equation is invoked (e.g. Stull, 1988), but used with a common parameterization of its terms (Stevens et al., 2000). In that way the following equation is found to be useful:

$$\frac{\partial TKE}{\partial t} = -\left[\frac{1}{a\cos\varphi}\left(u\frac{\partial TKE}{\partial \lambda} + v\cos\varphi\frac{\partial TKE}{\partial \varphi}\right)\right] - \dot{\varsigma}\frac{\partial TKE}{\partial \varsigma} - K_h N^2 + K_m DEF^2 - c_\varepsilon \frac{\varepsilon^{3/2}}{\Lambda} + \ldots$$

$$\ldots \frac{1}{a\cos\varphi}\frac{\partial}{\partial \lambda}\left(2K_m \frac{\partial TKE}{a\cos\varphi \partial \lambda}\right) + \frac{1}{a\partial\varphi}\left(2K_m \frac{\partial TKE}{a\partial\varphi}\right) + \frac{g\rho_0}{\sqrt{\gamma}}\frac{\partial u}{\partial \varsigma}\left(2K_m \frac{g\rho_0}{\sqrt{\gamma}}\frac{\partial TKE}{\partial \varsigma}\right) \quad (31)$$

where *DEF* is again deformation and ζ vorticity. Here the TKE-equation is written in spherical coordinates and with the aLMo-specific vertical coordinate. Metrical terms are neglected. To complete the determination of the turbulence coefficients in Equations (29) and (30), the stability functions must be known. They form a stability-dependent Prandtl number. These functions have been derived from an extended Smagronsky-type subgrid-scale model (Manson and Brown, 1999). Finally, the length scale Λ, is related to grid spacing as a measure of the numerical resolution and is multiplied by a corrective factor. For more details we refer to Herzog et al. (2002). Kennedy and Shapiro (1980) claim further that the direct measure of K_m and K_h should prove useful for numerical models of frontogenesis.

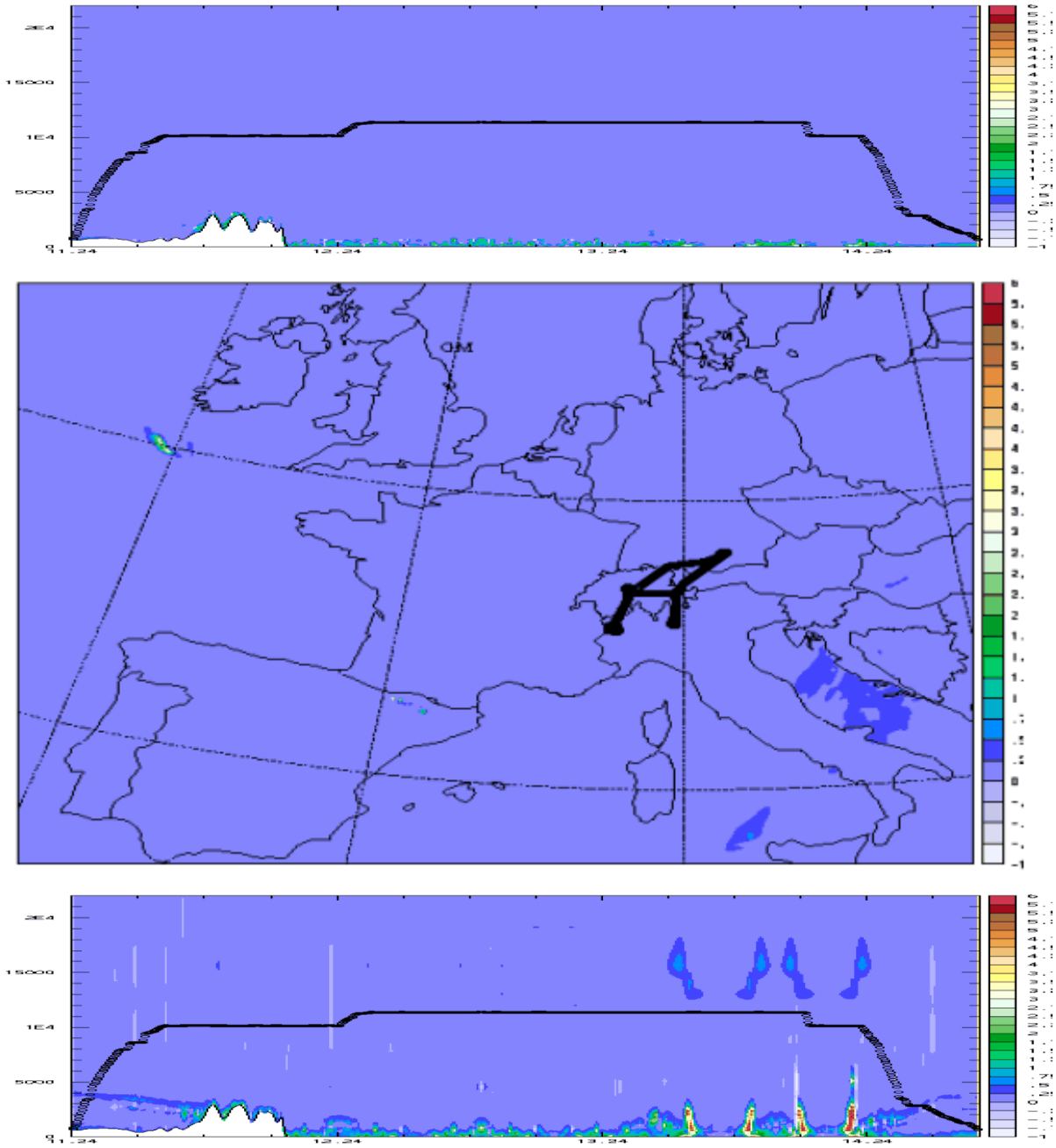

Figure 23: the upper panel is the same as the lower panel of Figure 21, i.e. diagnostic TKE, but for the Falcon MAP flight on 11th of November 1999 (see Figure 5). Both lower panels are prognostic turbulent kinetic energy, *PTKE*, charts for this Falcon MAP flight.

The prognostic turbulent energy field is currently only available for the MAP flights as additional aLMo simulations had to be performed, because this prognostic parameterization also influences other aLMo meteorological fields.

The two lower panels of Figure 23 show examples of this prognostic turbulent kinetic energy (PTKE) field for the MAP Falcon flight on 11th of November 1999. The synoptic situation on that day was as follows. A strong northerly jet (wind velocity greater than 50 m/s at 300 hPa) advects eastwards from western France (0 UTC) and reaches the eastern Alps at around 9 UTC. Now the jet axis is tilted from north to north-west ensuring for the second half of the day strong flow across the Alps.

6.12 Not considered indicators

One indicator that was not considered in the present study is the index proposed by Dutton (1980), who carried out multiple linear regression analyses to identify the combination of indices which exhibits the best linear relationship with reported CAT. The following empirical index (*E*) has emerged as the best predictor of CAT:

$$E = 1.25 \cdot S_H + 0.25 \cdot S_V^2 + 50 \quad (32)$$

where S_H denotes the horizontal wind shear given defined as:

$$S_H = \frac{1}{V^2}\left(uv\frac{\partial u}{\partial x} - u^2\frac{\partial u}{\partial y} + v^2\frac{\partial v}{\partial y} - uv\frac{\partial v}{\partial y} \right) \quad (33)$$

Attempts to improve on the regression equation by the inclusion of topography (as held in the numerical model) have proved disappointing; no significant improvement in the skill of the CAT index was evident.

Scorer (1963) first derived an expression for the rate of change of the Richardson number following the motion in a standing gravity wave which enabled predictions to be made about where turbulence would develop with respect to the trough-crest pattern.

Roach (1979), Brown (1973) and Keller (1990) all propose turbulence indicators based on, or directly employ the Richardson tendency equation. Following Keller (1990), the total *Ri* tendency equation is defined as the time rate of change of ln(*Ri*) following the motion. In general, both its nonturbulent and turbulent components must be considered, so that

$$\frac{D}{Dt}\ln(Ri) = -\Phi - \xi \quad (34)$$

where the nonturbulent component, Φ, is a result of shearing and stretching deformation associated with meso-alpha and synoptic scale disturbances in the upper troposphere. Atmospheric processes acting to modify ln(*Ri*) and attributed to ξ are due to the unresolvable subgrid phenomena associated with CAT; these include KHI with horizontal scales of a few km and random turbulent eddies of a few tens or hundreds of meters. The explicit form of the turbulent and nonturbulent term is given in Keller (1990).

Equation (34) has not been considered because of two main reasons: first because this equation is very useful when only present data are available in order to make forecast, but here we wanted to use the forecast already computed by the mode,l and second because often negative values of the Richardson number were detected in every aLMo output, which of course does not allow the computation of the Richardson tendency.

Sharpiro (1978) proposed the potential vorticity gradient as an index. This index was not considered neither.

Finally the non-linear balance equation (NBE), derived from the full divergence tendency equation in the case that its advection, the non-linear effects of divergence and the contributions of vertical motion gradients can be neglected, is also a measure of the flow's imbalance, and is given by Knox (1997):

$$2J(u,v) - \beta u + f\zeta - \nabla^2\Phi \quad (35)$$

where J stays for the Jacobian, ζ is the relative vorticity, f is the Coriolis parameter, and $\nabla^2\Phi$ stands for the horizontal Laplacian of the geopotential. Deviations from this balance condition, i.e. the residuum of Equation (35), are also a measure for the flow's potential instability. As underlined by Knox (1996), strong anticyclonically curved flows may be regions with large vertical shears. These regions, by means of geostrophic adjustment and inertial instability offer mechanisms for GW generation. Therefore the residual of the NBE (Equation 35) could also be a good indicator, which was not considered in this study. However, Kronebach (1964) who classified 593 turbulence reports with respect to ridges and troughs noted that three times as much occurred under cyclonic conditions as under anticyclonic conditions.

7. Correlation between aLMo indicators and observational turbulence intensities

As a first simple measure of the indicators ability to forecast turbulence, we simply compute the correlation between observed turbulence intensities as given by ε and the several aLMo turbulence indicators. The correlation between a set of observations o and the same number of forecasts y is defined as the ratio of the sample covariance of the two variables to the product of the two standard deviations:

$$r_{oy} = \frac{\mathrm{cov}(o,y)}{s_o s_y} = \frac{\frac{1}{n-1}\sum_{i=1}^{n}(o_i-\bar{o})(y_i-\bar{y})}{\left[\frac{1}{n-1}\sum_{i=1}^{n}(o_i-\bar{o})^2\right]^{1/2}\left[\frac{1}{n-1}\sum_{i=1}^{n}(y_i-\bar{y})^2\right]^{1/2}} \quad (36)$$

This correlation, or Pearson correlation, is neither robust nor resistant. It is not robust because strong but nonlinear relationships between the two variables o and y may not be recognized. It is not resistant since it can be extremely sensitive to one or a few outlying point pairs.

The Pearson correlation coefficient has an important property: it is bounded by $-1 \leq r_{oy} \leq 1$ with $||r_{oy}||=1$ for a perfect (anti-)correlation and 0 for uncorrelated parameters. The correlation coefficient provides no explanation about the relationship between the variables and the causes of the correlation.

In this first comparison between aLMo turbulence indicators and turbulence intensities derived from aircraft observations we proceed in the following way. We look at both turbulence intensities along an entire flight. One difficulty to overcome is that there are N=256 aLMo indicator values for one derived EDR value. Therefore, two methods have been tested for this single flight approach.

First, we computed the correlation of the EDR array with each of the N corresponding aLMo indicators array, leading to N correlations for every aLMo indicator. Then, for every indicator, we take the value which shows the highest correlation, the mean value and the median value. The correlations are displayed on the same line as the descriptor's acronym in the left part of Figure 24 (Swss flight number 4) and 25 (MAP Falcon flight). Secondly we correlate the EDR values with each of the minimum, the maximum, the mean and the median value of the N indicators values and take the best of those four "skills". This correlation along with the method having best correlation (min, max, mea and med) is displayed in the mentioned images just below the correlation from the first methodology.

The correlations, for the single Swiss flight on 11th March 2004, shown in Figure 24, are high for most indicators except for *NSQ* (r_{oy}=-0.4) and *Ri* (r_{oy}=-0.3). As the *Ri* indicator has a very broad numerical distribution, it might have been of advantage to correlate ln(*Ri*) rather than *Ri*, following an analogous idea as in Equation (34).

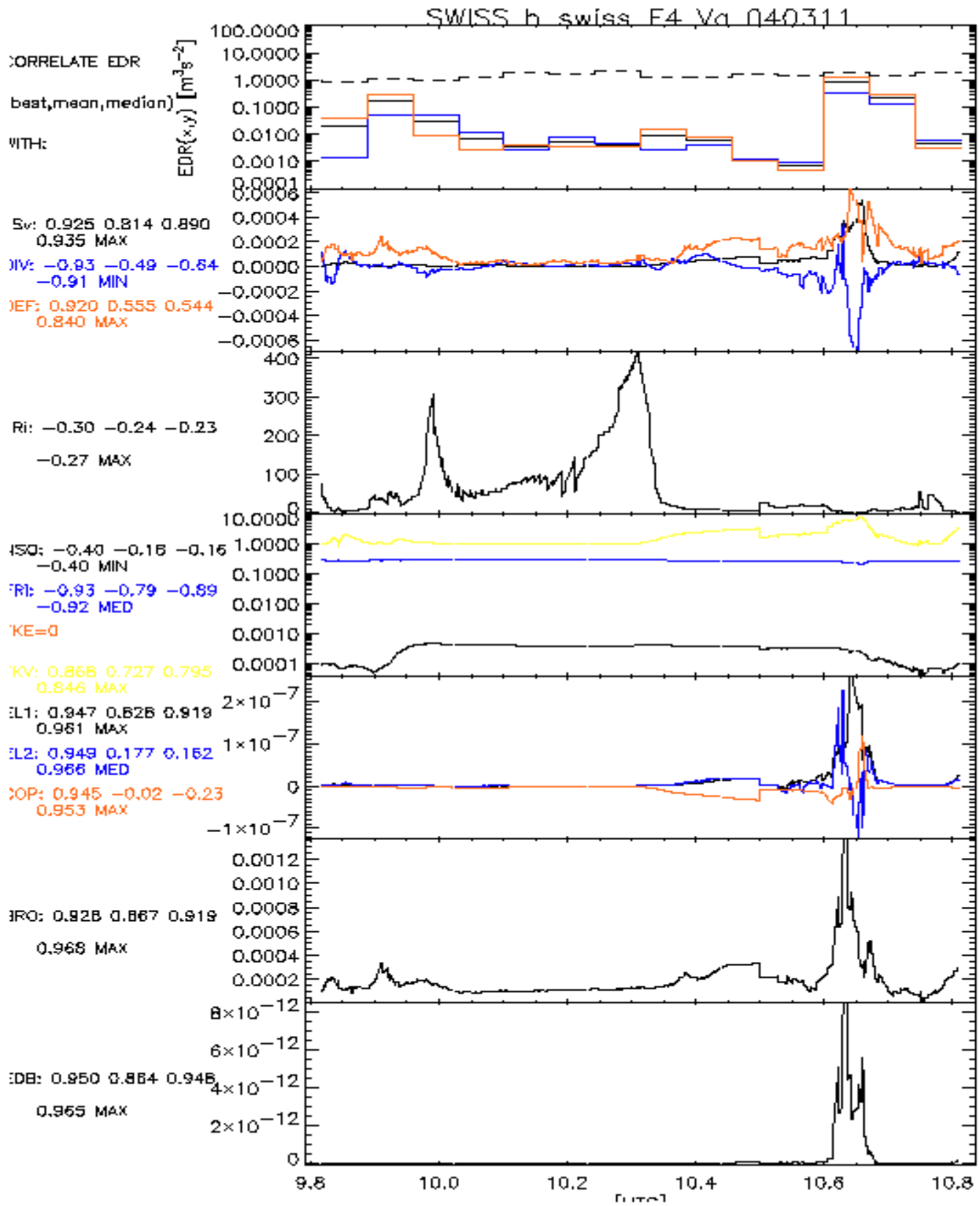

Figure 24: upper panel as third panel of Figure 4: EDR values from plane observations. All other panels display aLMo indicators interpolated to the plane location. The labeling in the left column denotes, for each indicator, the maximum, mean and median of all correlations between each *N=256* indicator values and the EDR values (upper line) and (lower line) the best correlation value when taking the minimum, maximum, mean or median value within the N=256 segment and the best method.

Note that for this flight the best forecast indices are *EDB, BRO, EL2 EL1* and *COP*, thus all indicators belonging to category of indices derived in a specific turbulence forecasting objective.

The correlations shown in Figure 25 for the longer Falcon MAP flight on 8th March 1999 are much lower. *FRi* and *EDB* show the best skills for this flight.

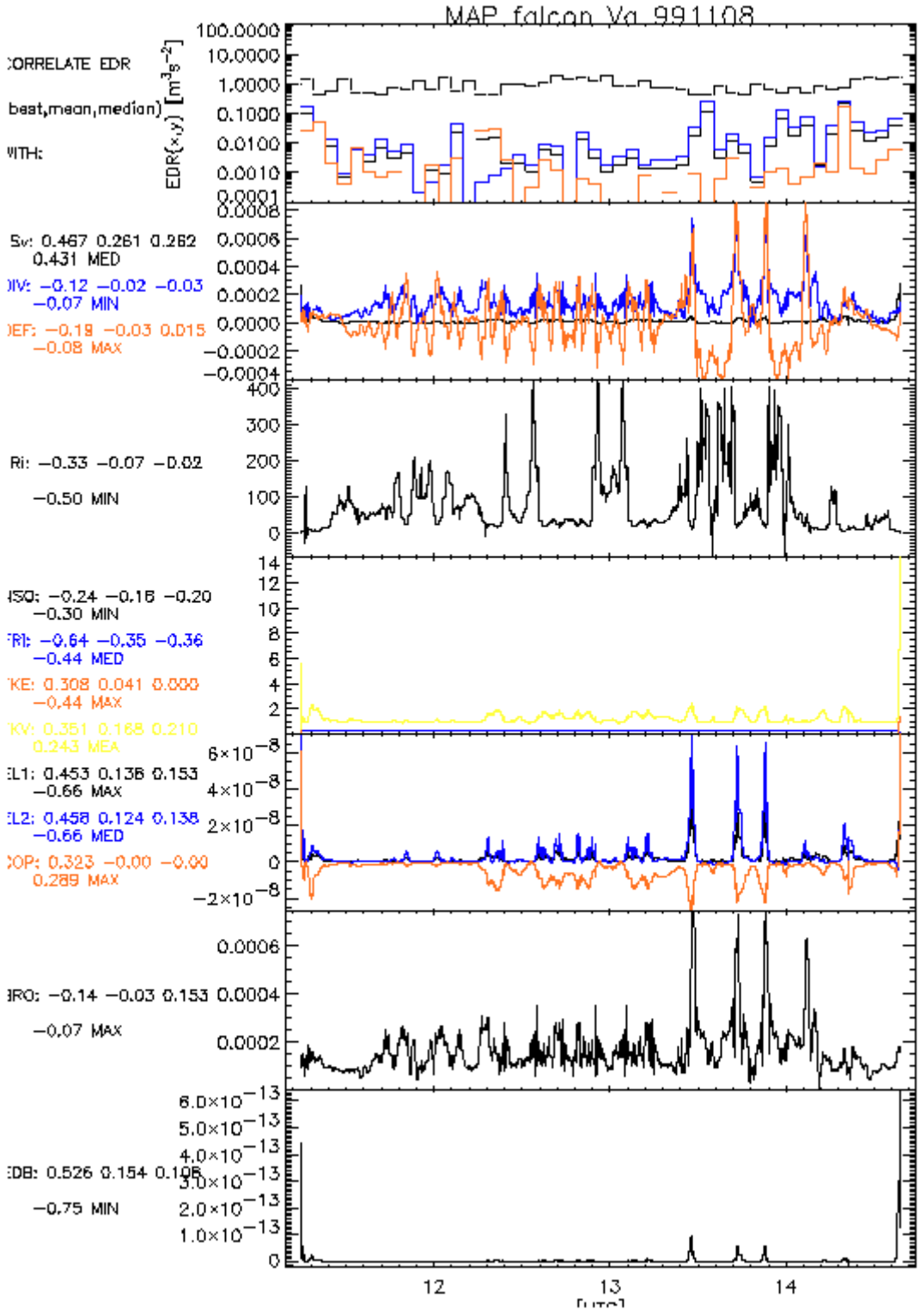

Figure 25: Same as figure 20 but for the falcon MAP flight on 11th of November 1999 (see also figure 5)

As the method computing the correlation for every N =256 aLMo values requires intensive computations, as there is little physical justification for it and as there seems to be good correspondence between the best methodology for most of the indicators of Figure 24 and 25, in the following, we will carry on only the second methodology, that is aLMo data reduction prior to compute the correlations.

Always looking at single flights, Figures 26 and 27, display the best correlation between the observed ε and the aLMo indicators (from the minimum, the maximum, the median and the mean of each 256 values of an aLMo indicator). For both data sets a great variability of the indicators is found. Further investigation is needed to determine the causes of these large changes in the correlation. One suspicion is that the bad forecasted flights are flights with encounters of much severe turbulence. Note that the considered Swiss flight number 4, along with e.g. F7 is among the flights the turbulence encounters of which were good forecasted.

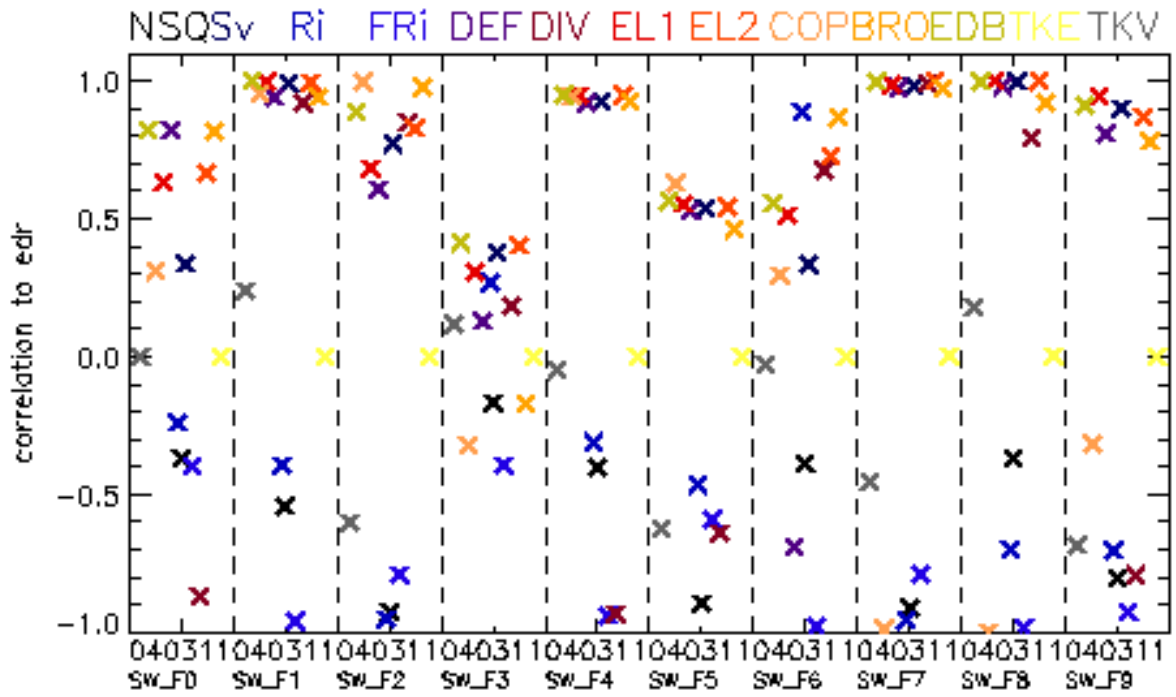

Figure 26: EDR to aLMo indicators (listed above) correlation for 10 selected Swiss flights.

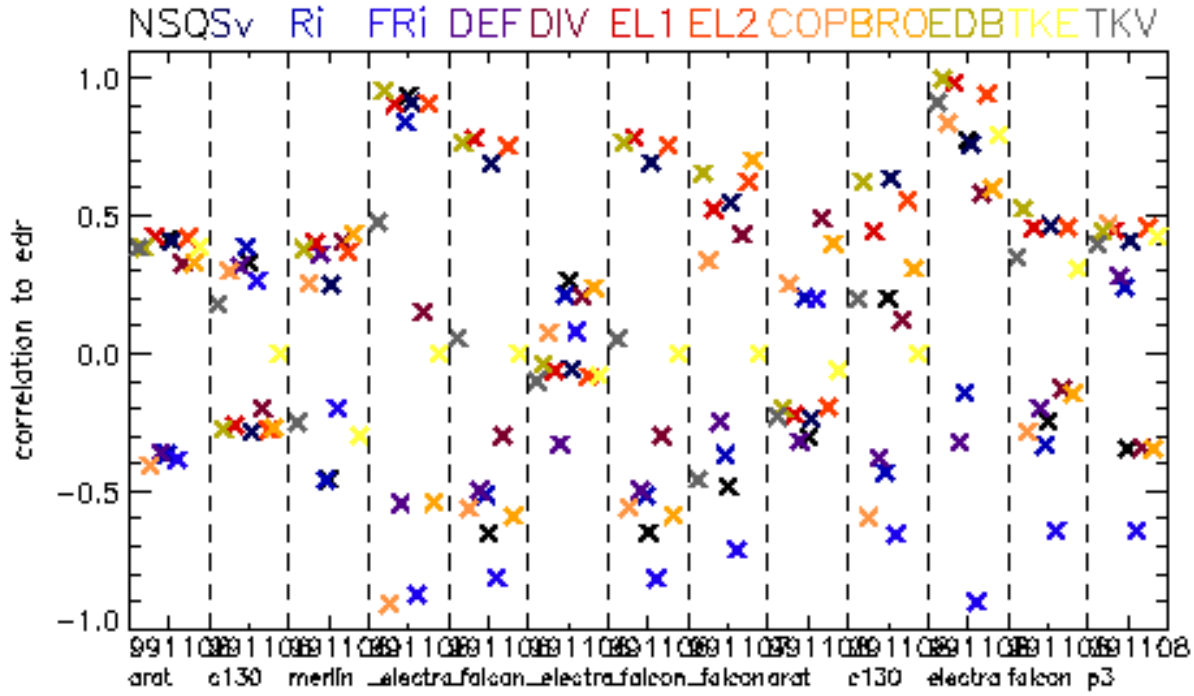

Figure 27: EDR to aLMo indicators (listed above) correlation for 13 selected MAP flights.

The tendency observed in Figures 24 and 25 for a single flight, seems to be confirmed when comparing Figure 26 and 27, namely that the turbulence encountered by MAP flights is generally less well forecasted than for the Swiss data set. A further noticeable point is that the indicators *Ri* and *FRi* for some flights, as the first C130 the second Electra and the Arat flight in Figure 27, the correlation with the Eddy dissipation rate changes sign and becomes positive. This is a further illustration of the difficulty of forecasting turbulence as it is true that the Richardson number is often seen as one of the best indicators.

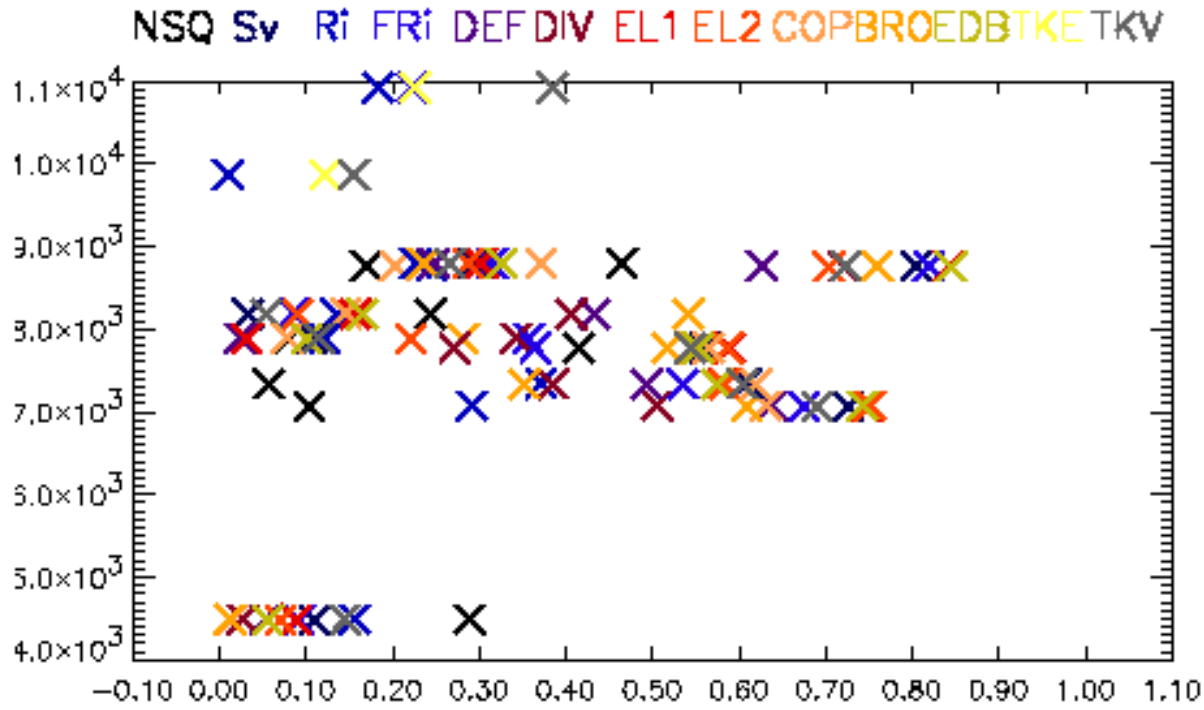

Figure 28: EDR to aLMo indicators (listed above) correlation for 10 selected Swiss flights as function of the aircraft mean cruise altitude.

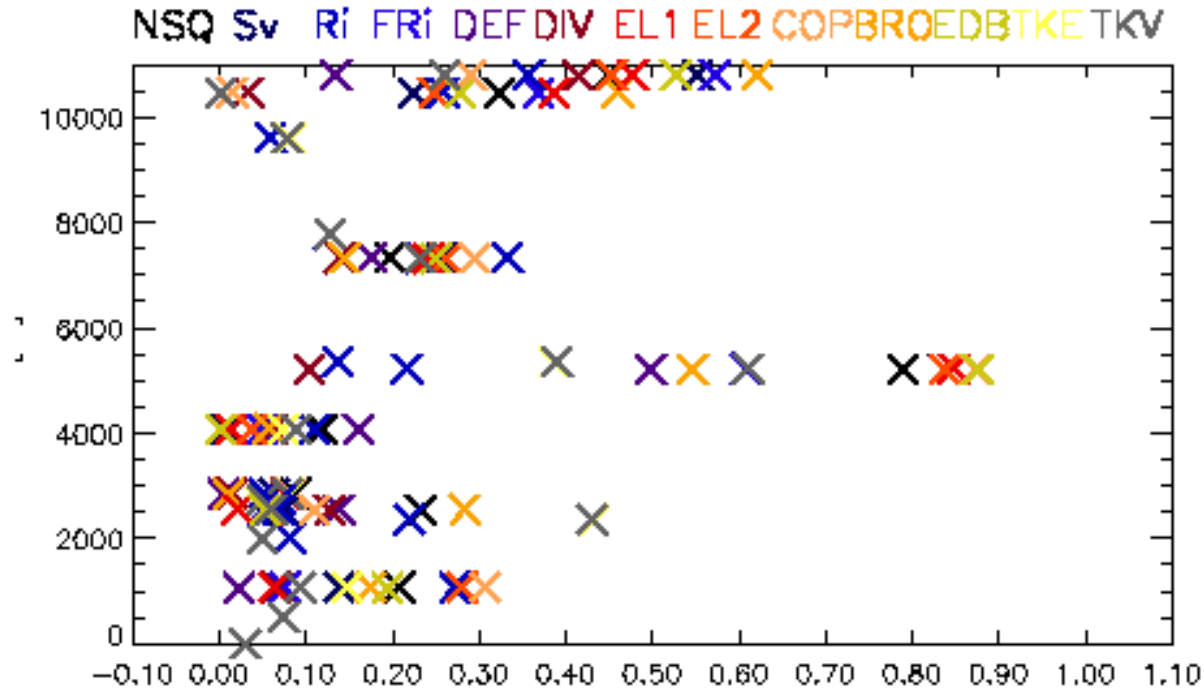

Figure 29: EDR to aLMo indicators (listed above) correlation for 13 selected MAP flights as function of the aircraft mean cruise altitude.

Then the same correlations plotted in Figures 26 and 27 were displayed as a function of airplane altitude (Figures 28 and 29 respectively) and as a function of aLMo forecast time (Figures 30 and 31 respectively).

Looking at both data sets, there seems to be a vertical range say between 5000 and 9000 m with best forecasts. For the considered MAP flights, the skill of the forecast seems to increase again above 10000 m. Here again further investigation would be required for a better assessment.

The expected relation of better forecast with smaller aLMo forecasting time seems to be found when looking at Figures 30 and 31, at least what concerns the MAP data set. It has been shown in many other studies e.g. in the study of Bysouth (2000) that there is a lack of skill in CAT forecsts created directly from model output between 18 and 24h forecast time. Bysouth (2000) in her study on short range clear air turbulence forecast, found that there is no clear advantage in simply shortening the lead-time of these forecasts. In some cases, their forecast are improved but it has a detrimental effect on many of the best forecasts due to the smoothness of the wind field early on in the life cycle of the forecast, i.e. in the very first hours.

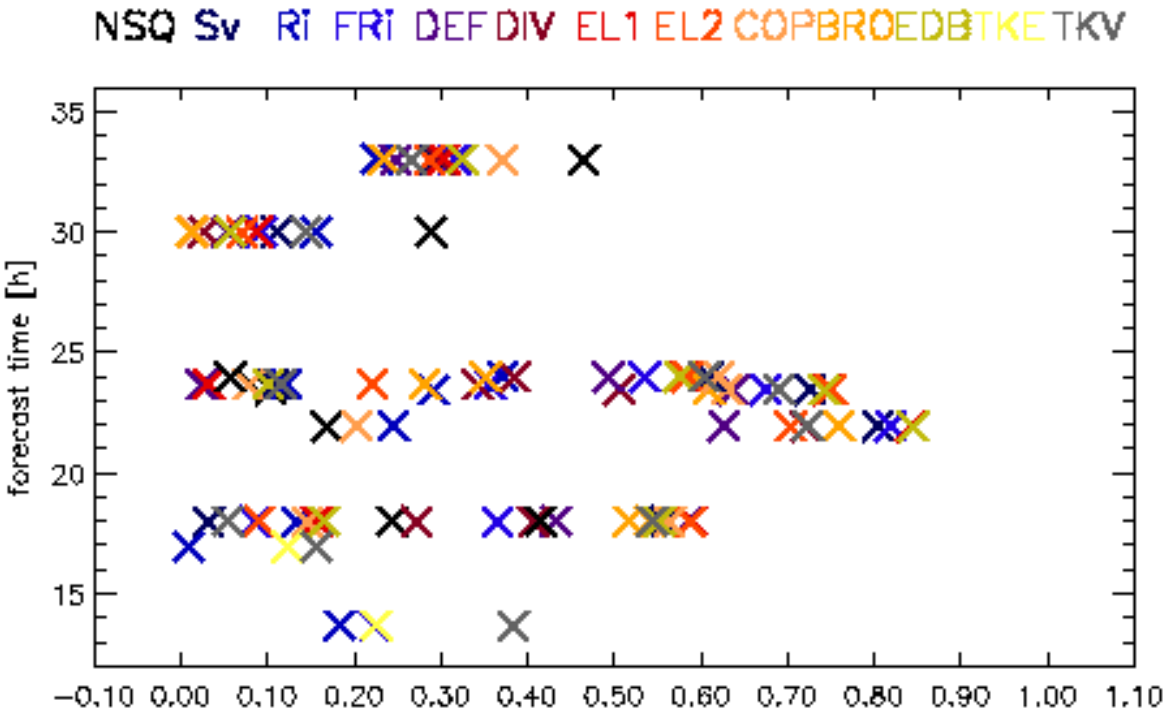

Figure 30: EDR to aLMo indicators (listed above) correlation for 10 selected Swiss flights as function of the forecast time of the aLMo simulation.

These first correlations pinpointed to the difficulty to find any correspondence or any general law about the accuracy of the considered aLMo indicators about forecasting turbulence. In the following, in a further attempt for an unequivocal ranking, two skill score measures will be applied to every available flight from both data sets.

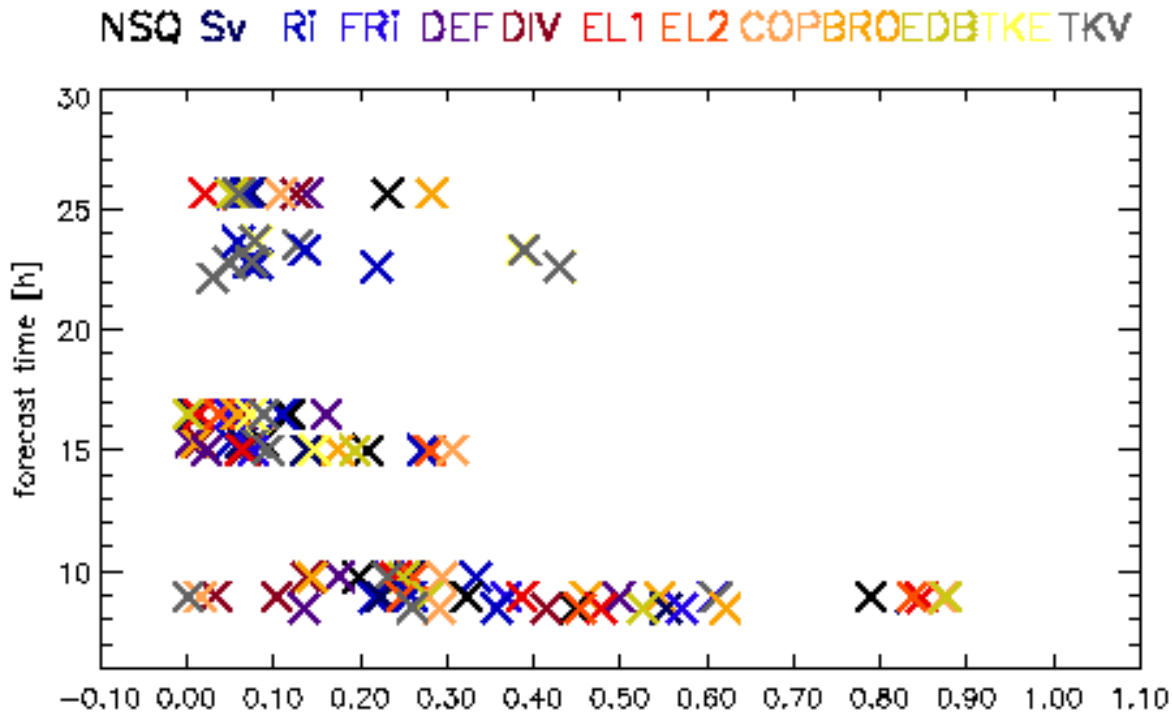

Figure 31: EDR to aLMo indicators (listed above) correlation for 13 selected MAP flights as function of the forecast time of the aLMo simulation.

8. Ranking of the turbulence indicators

In the present section, the considered turbulence indicators are being inter-compared and ranked with respect to their forecast skill. In order to compute these skill score measures of the turbulence indicators, a data reduction of the N=256 interpolated values of the aLMo indicators, corresponding to an EDR observation was applied, namely by means of the following four methods: the minimum value (in the following also mi), the maximum value (ma), the mean value (mn) and the median value (med). Here only the method leading to the best score for a given indicator has been considered.

The next step to be undertaken in order to rank the different turbulence indicators is to classify them in bins, as are the observational turbulence intensities. Therefore, the aLMo indicators were first distributed in five classes following the relative frequencies of the observational EDR values (see Table 1), taking into account the sign of the correlation. For the divergence field, its absolute values have been taken leading to a non-differentiation between convergence and divergence. The result is that every indicator's values are now attributed to one of five turbulence intensities with the same relative frequencies as for the observed turbulence. For example, the numerical value delimiting extreme from severe turbulence for the Richardson number was set to 0.66 following the median method.

Alternatively, another verification scheme is implemented to verify if the parameters are able to distinguish the two classes: turbulent and non-turbulent flow. In the case of the Richardson indicator with the median method again.

By means of these adjoint distributions (from observations and for every single aLMo indicator), contingency tables, as shown in Table 5 for the 2x2 case, can be built for different numbers of classes: 5x5, 4x4, 3x3, and 2x2; where a, b ,c and d are the count of events over all flights.

The chosen numerical values of the boundaries for the observed EDR are listed in Table 1 for the 5x5

case and in Table 6 for all other cases.

Table 5: Schematic 2x2 contingency table. a to d are number of corresponding events.

		observation yes	no
forecast	yes	***a***	***b***
	no	***c***	***d***

Table 6: Numerical values of the boundaries delimiting turbulence intensities for the observational EDR, for 4, 3 and 2 turbulence classes.

Number of classes	***Class 1***	***Class 2***	***Class 3***	***Class 4***
4	<0.1	0.1-0.3	0.3-0.5	>0.5
	nil	light/moderate	moderate/severe	extreme
3	<0.3	0.3-0.5	>0.5	
	nil/light/moderate	moderate/severe	extreme	
2	<0.3	>0.3		
	non-turbulent	turbulent		

Commonly, forecast verification data in contingency tables are characterized by using relative accuracy measures, or skill scores. All possible skill scores are scalar measures of forecast performance in what is intrinsically a higher-dimensional setting. Five different skill measures have been applied here to the different aLMo indicators. The first is simply the mean absolute error (MAE).

$$MAE=\frac{1}{n}\sum_{i=1}^{n}|y_i-o_i| \quad (35)$$

where $p(o_i)$ and $p(y_i)$ are the observational probability and the forecast probability of event i respectively of n observations. A perfect forecast of an indicator would result in a MAE of zero. The greater MAE is, the worse the skill of an indicator. The mean absolute error will be shown exemplarily in table 11. One disadvantage of this skill measure is that it should be used mainly for metric variables. Applied to classified data the interpretation becomes difficult.

The second forecast accuracy measure is the Kuipers skill score (KSS) for which the reference hit rate in the denominator is that for random forecasts that are constrained to be unbiased. That is, the imagined random reference forecasts in the denominator have a marginal distribution that is equal to the (sample) climatology. The Kuipers skill score is computed for *IxJ* (*I=J=5,4,3,2* in our case) different classes as

$$KSS=\frac{\sum_{i=1}^{I}p(y_i,o_i)-\sum_{i=1}^{I}p(y_i)\,p(o_i)}{1-\sum_{j=1}^{J}\left[p(o_j)\right]^2} \quad (36)$$

where $p(y_i,o_i)$ is the joint distribution of the forecasts and observations. The reader is referred to Wilks (1995) e.g. for different possible notations of this joint distribution. Here, we only show the form for two classes:

$$KSS = \frac{2(ad - bc)}{(a+c)(c+d)+(a+b)(b+d)} \quad (37)$$

where *a,b,c* and *d* are defined according to Table 5.

The third measure is the Heidke skill score (HSS). It is formulated similarly to the Kuipers score, except that the reference hit rate in the denominator is different (Wilks, 1995):

$$HSS = \frac{\sum_{i=1}^{I} p(y_i, o_i) - \sum_{i=1}^{I} p(y_i)\,p(o_i)}{1 - \sum_{i=1}^{I} p(y_i)\,p(o_i)} \quad (38)$$

and in the case of a 2x2 contingency table, the Heidke skill score reduces to:

$$HSS = \frac{ad - bc}{(a+c)(b+d)} \quad (39)$$

With the Kuipers or the Heidke skill score, a perfect forecast receive a score of one, random forecasts receive a score of zero, and forecasts inferior to the random forecasts receive negative scores.

Unlike the Heidke score, the *KSS* posess the appealing characteristic that the contribution of a correct forecast increases as the event is more or less likely. Thus forecasters are not discouraged from forecasting rare events on the basis of their low climatological probability alone.

From the definitions of the Kuipers and the Heidke score, it is apparent that both scores are equal in the case that

$$\sum_{i=1}^{I} o_i \Big|_{j=a} = \sum_{j=1}^{J} y_j \Big|_{i=a} \quad a = 1,...,I \quad (40)$$

Or in the case of two classes (see table 5) both scores are equal if

$$a + c = a + b$$
$$b + d = c + d \quad (41)$$

The two indicators provide thus the same results if the number of events in the classes are the same for each computed turbulence indicator and for the measured EDR values. An alternative view is that the sum on every row in the contingency table is equal to the sum on its corresponding column, and hence the denominators of both skill scores are equal. This is true for all the following contingency table investigations and therefore only the KSS is shown in the following tables. Only in table 13 both skill scores will be displayed as we compare there the EDR value additionally to the indicator's value for the preceding and following time step and therefore Equation (40) is not satisfied anymore for this special case.

For the accuracy of categorical forecasts in 2x2 contingency tables two additional measures have been calculated. The first is called the probability of detection (POD), which is simply the fraction of those occasions when the forecast event occurred and for which it was also forecasted to all occurred events:

$$POD = \frac{a}{a+c} \quad (42)$$

That is, the likelihood that turbulence is forecasted correctly, given that it was measured. The POD for perfect forecasts is one, and for no correct forecast, the POD is zero.

The last measure is the complement of the probability that turbulence occurred given that it has been forecasted, which is known as the false-alarm rate (FAR):

$$FAR = \frac{b}{a+b} \quad (43)$$

Again its values are from zero to one, whereas for this measure the best score is zero, no false alarm.

In the case that Equation (40) is satisfied the sum of POD and FAR is exactly 1. The larger the POD and along with, the smaller the FAR is, the more the indicator yields an accurate forecast.

The following tables display the KSS scores for a 5x5 contingency table for MAP data (table 7), for Swiss data (table 8) and for both data sets taken together (table 9) following the turbulence classification shown in table 1.

Table 7: Ranking of the 12 aLMo indicators with Swiss observations.

aLMo Ind.	KSS rank	KSS score	KSS meth
FRi	**1**	**0.117**	**mn**
BRO	**2**	**0.11**	**ma**
EL1	**2**	**0.11**	**mn**
COP	2	0.11	ma
NSQ	5	0.092	mi
DEF	5	0.092	ma
Ri	7	0.082	med
EDB	8	0.075	ma
EL2	8	0.075	ma
TKV	10	0.068	ma
Sv	11	0.065	ma
DIV	12	0.054	mn

Table 8: Ranking of the 13 aLMo indicators with MAP observations.

aLMo Ind.	KSS rank	KSS score	KSS meth
FRi	**1**	**0.192**	**mn**
NSQ	**2**	**0.189**	**mi**
Ri	**3**	**0.184**	**mn**
COP	4	0.163	mn
EDB	5	0.158	mn
DEF	6	0.147	mi
EL1	7	0.146	med
EL2	7	0.146	med
BRO	9	0.14	ma
Sv	10	0.132	ma
TKV	11	0.122	ma
DIV	12	0.072	ma
TKE	13	0.059	ma

Note that the displayed methods (meth) in tables 7 to 13 indicate which of minimum, maximum, mean or median of the 256 aLMo indicator data points achieved the best score. The outstanding feature when comparing the skills of the parameters with the two datasets separatly is the much better scores of the parameters when considering MAP data alone, despite worse correlation. One possible reason might be the lower quality of the Swiss wind measurements, but further investigation is needed to

confirm this impression. Some coherence between the tables can be found. In both cases the FRi parameter (Flux Richardson number, see Equation 17) seems to be the best.

The skill scores are positive, hence there can be at least some skill expected of the model forecasts.

An alternative approach would have been, instead of using the aLMo data corresponding to the previous and next flight lag, to define a volume around the observational section and retrieve aLMo data within this volume for the previous, momentary and next time step.

When looking at the turbulence indicators for both datasets, the *FRi* still shows the best result, followed by the static stability, *EDB*, *COP* and *BRO*. The gook rank of the squared Brunt Väisälä Frequency, *NSQ*, might surprise, but when considering that in turbulent spots *NSQ* tends to zero, one recognizes that *NSQ* might in effect be a good turbulence diagnostic, especially when taking the minimum value, as is the case in table 7 to 11.

In tables 9 to 12, the five best indicators following the KSS for contingency tables with numbers of rows and columns successively reduced from 5 to 2 are shown. As a result, the skill score continuously increases as the number of classes is reduced. Note the large coherency of the displayed best parameters. *FRi* is in three times best and in one case second, *NSQ* twice second and twice third and *COP* is also consistently near or at the pole position. *Ri* reaches the fourth rank when the turbulence is classified in three or two bins.

Of high practical value are the results in table 11 because the forecaster has to detect either moderate or severe turbulence.

Table 9: Ranking of the 5 best aLMo indicators in five classes with Swiss and MAP observations together.

aLMo Ind.	KSS rank	KSS score	KSS meth
FRi	**1**	**0.183**	**mn**
NSQ	**2**	**0.17**	**mi**
EDB	**3**	**0.167**	**ma**
COP	4	0.16	md
BRO	5	0.151	ma

Table 10: As Table 9, but for four turbulence classes (see Table 6).

aLMo Ind.	KSS rank	KSS score	KSS meth
FRi	**1**	**0.201**	**mn**
COP	**2**	**0.185**	**mn**
NSQ	**3**	**0.183**	**mi**
EDB	4	0.172	ma
EL1	5	0.164	ma

Table 11: As Table 9, but for three turbulence classes (see Table 6).

aLMo Ind.	KSS rank	KSS score	KSS meth	MAE	MAE meth
FRi	**1**	**0.245**	**mn**	**0.114**	**mn**
NSQ	**2**	**0.224**	**mi**	**0.119**	**mi**
COP	**3**	**0.214**	**med**	**0.121**	**med**
Ri	4	0.193	med	0.124	med
TKV	5	0.155	mi	0.133	ma

Table 12: As Table 9, but for two turbulence classes (see Table 6) and with two further skill scores.

aLMo Ind.	rank	KSS score	method	FAR	method	POD	method
COP	**1**	**0.294**	**med**	**0.669**	**med**	**0.331**	**med**
FRi	**2**	**0.287**	**mn**	**0.675**	**mn**	**0.325**	**mn**
NSQ	**3**	**0.28**	**mn**	**0.682**	**mn**	**0.318**	**mn**
Ri	4	0.252	med	0.709	med	0.291	med
TKV	5	0.182	ma	0.775	ma	0.225	ma

Table 11 further displays the mean absolute error, the ranking of which is found to be consistent with the KSS ranking. It can be noted that the MAE is small which is mainly due to the large amount of data in the contingency table corresponding to no turbulence forecasted and no turbulence observed. As mentionned, MAE does not take into account the likeliness of a particular event.

For all contingency tables the skill scores are modest due to the fact, that the turbulence intensity is usually zero and the model seems to have problems to detect the rare turbulent events at the exact time. Logically, the less restrictive the classification is, the better the skill scores are.

In the case of turbulent/non turbulent forecast (table 12) the skill reaches approx. 0.3; compared to skill scores of other model forecasted parameters such as temperatures this is a rather modest result. However, for a turbulence forecast this is already a quite good record.

The used dataset, which consists of 148 swiss flights and 19 MAP flights, was subdivided into three datasets to investigate if the results strongly depend upon the considered flights. The ranking order of the indicators is not always the same, but the ranking is very similar to those displayed in tables 9 to 12. This verification further pinpoints to the robustness of our results.

To further assess the accuracy of the aLMo forecasting events with turbulence, a very simple approach has been investigated. Due to the fact that the model seems to have problems to detect events with higher turbulence (EDR > 0.3) at the exact time, the measured and the forecasted values have not only been compared at the same time interval and location but also at the immediate preceding and following one along the flight track. An observation distance crossed by the planes of 150-200 km is thus now considered. An alternative approach would have been, instead of using the aLMo data corresponding to the previous and next flight lag, to define a volume around the observational section and retrieve aLMo data within this volume for the previous, momentary and next time step.

This investigation has only been done for a 2x2 contingency table. Here the KSS, HSS, FAR and the POD have been calculated and are shown in table 13. The EDR threshold delimiting turbulent from non-turbulent flow is as for table 12 of 0.3.

The approach of investigating larger flight intervals leads now to different counts in the turbulence intensity classes for the measured and modelled data. Therefore the sum of POD and FAR may not equal 1 any more and the HSS and KSS differ and thus both are shown. The resulting values are now representative for much larger areas.

Table 13: KSS, HSS, FAR and POD of the 5 best aLMo indicators for Swiss and MAP observations with two turbulence classes. The values are now representative for a time period three times longer. The Ranking is the average ranking of all four measures.

aLMo Ind.	Total rank	KSS	method	HSS	method	FAR	method	POD	method
NSQ	**1**	**0.432**	**mn**	**0.454**	**mn**	**0.543**	**mi**	**0.457**	**mn**
COP	**2**	**0.419**	**med**	**0.443**	**med**	**0.556**	**med**	**0.444**	**med**
FRi	**3**	**0.392**	**mn**	**0.420**	**med**	**0.543**	**mn**	**0.**417	**mn**
Ri	4	0.368	med	0.406	med	0.589	med	0.391	med
DEF	5	0.335	mi	0.405	mi	0.662	ma	0.351	mi

The large increase in skill scores of these results and those before seems to confirm the assumption that the model has difficulties to forecast events with high turbulence correctly in time and space. With the new approach, all measures provide better scores. The bests indicators (*NSQ*, *COP* and *FRi*) provide a POD of around 45% with a FAR of 55%. Nevertheless it has to be mentioned that the FAR values are high, which is a bothering feature for a possible turbulence forecast. Still, the skill scores now display values that enter in the range of useful forecasts.

The results from this chapter for possible turbulence forecasts with the aLMo can be summarized as follows: Using 256 second intervals to compare observations with forecasts, all classifications provide insufficient results. With a less restrictive way of comparing observations with forecasts, namely comparing not only at the immediate time, the skill scores, POD and FAR measures become much better. This also confirms the assumption that a larger volume around the aircraft position along the flight path for the interpolation of the indicators would lead to better results. But then the gained higher skill scores would result in a lower spatial resolution of the turbulence forecast.

Regarding all different above considerations, we can summarize the best indicators among those considered for turbulence indication with aLMo data are *FRi*, *NSQ* and *COP*.

Sharman et al. (2003) made a ranking of several turbulence indicators. Their ranking, excluding the indices which were not mentioned in the present study is as following: after their own NCAR integrated turbulence forecast algorithm (ITFA) they found the Richardson tendency equation, followed by the residuum of *NBE*, the first index of Brown, the potential vorticity gradient, the Colson-Panofsky indicator, Ellrod and Knapp second index, and finally the Richardson number. However, Kronebach (1964) found the Richardson number the best turbulence indicator of the ones he tested.

Another less extensive ranking of turbulence indicators was undertaken at the UK Met-Office (Bysouth, 1998). She compared both Ellrod and Knapp indicators (see Section 6.7), the first Brown index (see Section 6.9) and a modified Dutton's empirical index (see Section 6.10). Using CAT reports archive, FASTEX and ASDAR data. She found the following order based on correlation classification: *EL2*, *EL1*, *BRO* and the modified Dutton index.

9. Conclusions

«Les oscillations des corps se composent d'oscillations simples qui s'accomplissent sans se nuire.»
Baron J. Fourier

Starting from airborne horizontal wind measurements, turbulence intensities have been derived for over 150 flights over Europe and especially over the Alps. These observed turbulence strengths have

been compared with a non-exhaustive list of 13 turbulence parameters all derived from the meteorological fields of the aLMo non-hydrostatic mesoscale model. The skill of these parameters was evaluated and subsequently the turbulence indicators were ranked. The best scores are *FRi*, *NSQ* and *COP*. Their skill scores are such that they are positive and it can be expected that useful forecasts in a routine turbulence scheme using aLMo might be achieved.

For the moment only little help for the forecaster is available for issuing turbulence forecasts and warnings for the alpine region beside turbulence information derived from global models. An implementation of the best turbulence parameters in aLMo has therefore a high potential to bring added value for the routine services.

In order to produce operational turbulence forecasts, further tests are still required and some guidelines based on the present investigation are given in the following section.

10. Outlook

Some questions need further investigation prior to producing operational turbulence forecasts. It needs to be clarified how the best turbulence indicators perform compared with each other in a pre-operational setting. Do the parameters exhibit complementary information if used in a complex, synoptic forecasting approach? Do e.g. the best three indicators achieve the positive score during all turbulence events or, is one indicator reliable for certain special cases or origin of turbulence? This will help to decide on how many, which of and how to combine the aLMo turbulence indicator(s) which then, could be routinely computed and mapped.

The question of the air-space in which turbulence should be forecasted should be addressed as mentioned in section 8. As a result of the present study it seems useful to divide the airspace horizontally into 4 to 12 regions.

These issues taken into consideration, efficient routinely turbulence forecasts for civil aviation based on aLMo output will become tangible.

11. References

Bacmeister, J. T., Newman, P. A., Gary, B. L., and, Chan, K. R., **1994**: Mountain wave related turbulence in the stratosphere. Wea. Forecasting, **9**, 241-253.

Batchelor, G. K., **1953**: On the accuracy of wind measurements using an inertial platform in an aircraft, and an example of a measurement of the vertical mesostructure of the atmosphere, J. Appl. Met., **7**, 645-666.

Bretherton, G. K., **1969**: Waves and turbulence in stably stratified fluids, Rad. Sci., **4**, 1279-1287.

Brown, R., **1973**: New indices to locate clear-air turbulence, Meteor. Mag., **102**, 347-361.

Buss, S., Hertzog, A., Hostettler, C., Bui, T. P., Lüthi, D., and Wernli, H., **2003**: Analysis of a jet stream induced gravity wave associated with an observed ice cloud over Greenland, Atmos. Chem. Phys., **3**, 5875-5918.

Bysouth, C., **2000**: Short range clear air turbulence forecasting, Forecasting research technical report, No 316, Meteorological Office Bracknell, UK, 16 pp.

Bysouth, C., **1998**: comparison of clear air turbulence indicators, Forecasting research technical report, No 242, Meteorological Office Bracknell, UK, 25 pp.

Colson, D., and, Panofsky, H. A., **1965**, An index of clear air turbulence, Quart. J. R. Met. Soc., **91**, 507-513.

Cornman, L. B., Morse, C. S., and, Cunni, G., 1995: Real-time estimation of atmospheric turbulence severity from in-situ aircraft measurements, J. aircraft, **32**, 171-177.

Djurić, D., **1994**: Weather analysis, Prentice Hall, Englewood Cliffs, New Jersey, 304 pp.

Doms, G., and Schaettler U., **1999**: The Nonhydrostatic Limited-Area Model LM (Lokal-Modell) of DWD, Part 1: Scientific Documentation, (available from http://www.cosmo-model.org and under /home/klo/users/sbu/TURB_proj/LM_RI/lmscidoc.2.ps).

Dutton, M. J., **1980**: Probability forecasts of clear-air turbulence based on numerical model output, Meteor. Mag., **109**, 293-310.

Duttton, M. J., and, Panovsky, H. A., **1970**, Clear air turbulence: a mystery may be unfolding, Science, **167**, 937-944.

Eidsvik, K., Holstad, A., Lie, I., and, Utnes, T., A prediction system for local wind variations in mountainous terrain, Bound.-Layer Meteor., **112**, 557-586.

Ellrod, G. P., **1989**: An index for clear air turbulence based on horizontal deformation and vertical wind shear. Preprints, *Third Intl. Conf. on the aviation weather system*, Anaheim, California, Amer. Meteor. Soc., 339-344.

Ellrod, G. P., and Knapp, D. I., **1992**: An objective clear-air turbulence forecasting technique: Verification and operational use, Wea. Forecasting, **7**, 150-165.

Gossard, E. E., and Hooke, W. H., **1975**: Waves in the atmosphere, Developments in atmospheric Science, Elsevier Scientific Publishing Co., Amsterdam, 456 pp.

Hertzog, H.-J., Vogel, G., and Schubert, U., **2003**: Incorporating a 3D subgrid scale turbulence scheme in the 2.8km-version of the LM, COSMO-Newsletter, No 3, 195-197 (available from http://cosmo-model.cscs.ch/public/newsLetters.htm).

Hertzog, H.-J., Schubert, U., Vogel, G., Fiedler, A., and, Kirchner, R., **2002**: LLM - the high resolution nonhydrostatic simulation model in the DWD-project LITFASS, Part I, Modelling technique and simulation method. COSMO Technical Report, No 4, 68 pp (available from http://cosmo-model.cscs.ch/public/newsLetters.htm).

Hertzog, A., Souprayen, C., and Hauchecorne, A., **2001**: Observation and backward trajectory of an inertio-gravity wave in the lower stratosphere, Ann. Geophysicae, **19**, 1141–1155.

Hitchman, M. H., Buker, M. L., Tripoli G. J., Browell E. V., Grant W. B., Hostetler, C., McGee, T. J., and Burris, J. F., **2003**: Nonorographic generation of Arctic polar stratospheric clouds during December 1999, J. Geophys. Res., 108, D5, 8325, doi:10.1029/2001JD001034.

Højstrup, J., **1982a**: A simple model for the adjustment of velocity spectra in unstable conditions downstream of an abrupt change in roughness and heat flux, Bound.-Layer Meteor., **21**, 357-367.

Højstrup, J., **1982b**: Velocity spectra in the unstable planetary boundary layer, J. Atmos. Sci., **38**, 2239-2248.

Hopkins, R. H., **1977**: Forecasting techniques of clear-air turbulence including that associated with mountain waves, World Meteorological Organization, Technical note, No 155, 31 pp.

Kaimal J. C., and Finnigan, J. J, **1994**: Atmospheric boundary layer flows their structure and measurement, 0195062396, Oxford University Press, 304 pages.

Kao, S. K., and Sizoo, A. H., **1966**: Analysis of clear air turbulence near the jet stream, J. Geophys. Res., **71**, 3799-3805.

Katul, G. and Chu, C.-R., **1988**: A theoretical and experimental investigation of energy-containing scales in the dynamic sublayer of boundary-layer flows, Bound-Layer Meteor. **86**: 279-312.

Kennedy, P. J., and, Shapiro, M. A., 1980: Further encounters with clear air turbulence in research aircraft, J. Atmos. Sci., **37**, 986-993.

Kim, Y.-J., Arakawa, A., **1994**: Improvement of orographic gravity wave prarmetrization using a mesoscale gravity wave model, J. Atmos. Sci., **11**, 1875-1902.

Klemp, J., and Wilhelmson, R., **1978**: The simulation of three dimensional convective storm dynamics, J. Atmos. Sci., **35**, 1070-1096.

Knox, J. A., **1996**: Possible mechanisms of clear-air turbulence in strongly anticyclonic flows, Mon. Wea. Rev., **125**, 1251–1259.

Kolmogorov, A. N., **1941**: Dokl. Akad. Nauk SSSR **30**, 301.

Kronebach, G. W., **1964**: An automated procedure for forecasting clear air turbulence, J. Appl. Meteor., **3**, 119-125.

Ludlam, F. H., **1967**, Characteristics of billow clouds and their relation to clear air turbulence, Quart. J. R. Met. Soc., **93**, 419-435.

Lyons, R., Panovsky, H. A., and Wollaston, S., **1964**: The critical Richardson number and its implication for forecast problems, J. Appl. Meteor., **3**, 136.

MacCready, P. B., **1964**, Standardization of gustiness values from aircraft, J. Appl. Meteor., **3**, 439-449.

Mancuso, R. L., and, Endlich, R. M., **1966**: Clear air turbulence frequency as a function of wind shear and deformation, Mon. Wea. Rev., **94**, 581-585.

Mason, P. J., and Brown, A. R., **1999**: On subgrid models and filter operations in large eddy simulations, J. Atmos. Sci., **56**, 2101-2114.

McCann, D. W., 2004, Opaerational forecasting of breaking mountain waves, personal copy.

Miles, J. W., **1964**, Note on a heterogeneous shear flow, J. Fluid. Mech., **20**, 331-336.

Pavelin, E. J., Whiteway A., and Vaughan G., **2001**: Observation of gravity wave generation and breaking in the lowermost stratosphere, J. Geophys. Res., **108**, 5173–5179.

Peters, D., Hoffmann, P., and Alpers, M., **2003**: On the appearance of inertio-gravity waves on the North-Easterly side of an anticyclone, Meteor. Zeitschrift, **12**, 25–35.

Pinus, N. Z., Reiter, E. R., Shur, G. N., and Vinnichenko N. K., **1967**: Power spectra of turbulence in the free atmosphere, Tellus, **XIX**, 2, 206-213.

Raschendorfer, M., **2001**: The new turbulence parameterization of LM, Research reports, COSMO-Newsletter, No 1, 89-96 (available from http://cosmo-model.cscs.ch/public/newsLetters.htm).

Reiter, E. R., and, Foltz, H. P., **1967**: The prediction of clear air turbulence over mountainous terrain, J. app. Meteor., **6**, 529-556.

Roach, W. T., **1970**: On the influence of synoptic development on the production of high level turbulence, Quart. J. R. Met. Soc, **96**, 413-429.

Scorer, R. S., **1968**: Mechanics of clear air turbulence, Proc. Of Symposium on *Clear air turbulence and its relation to aircraft*, RAE Farnborough, 14-16 August 1968, Seattle, U.S.A., 22 pp.

Scorer, R. S., **1963**: The reduction of the Richardson number by mountain waves, Proc. Symp. on atmospheric turbulence and its relation to aircraft, RAE Farnborough, 16 November 1961, 156-168, HMSO.

Shapiro, M. A., **1978**: Further evidence of the mesoscale and turbulent structure of upper level jet stream-frontal zone system, Mon. Wea. Rev., **106**, 1100-1111.

Sharman, R., Wiener, G. and Brown, B., **2003**: Description and verification of the NCAR integrated turbulence forecasting algorithm, American Institute of aeronautics and astronautics, internal publication, AIAA-00-0493.

Sharman, R., Landau, D., and Wurtele, M. G., **2000**: Another approach to operational forecasting of mountain wave turbulence, internal publication, AIAA-2000-0491.

Shibata, T., Sato, K., Kobayashi, H., Yabuki, M., and Shiobara, M., **2003**: Antarctic polar stratospheric clouds under temperature perturbations by nonorographic inertia gravity waves observed by micropulse lidar at Suowa station, J. Geophys. Res., **108**, D3, 4105, doi:10.1029/2002JD002713.

Steverns, D. E., Bell, J. B., Almgrena, A. S., Beckner, V. E., and Rendlman, C. A., **2000**: Small-scale process and entrainment in a stratocumulus marine boundary layer, J. Atmos. Sci., **57**, 456-581.

Stull, R. B., **1988**: An introduction to boundary layer meteorology, Series: Atmospheric and Oceanographic Sciences Library, Vol. 13, 680 p., ISBN: 90-277-2768-6.

Taylor, G. I., **1931**: Effect of variation in density on the stability of superposed layers of fluid, Proc. Roy. Soc., A, **132**, 499.

Thomas, L., Worthington R. M., and McDonald, A. J., **1999**: Inertia-gravity waves in the troposphere and lower stratosphere associated with a jet stream exit region, Ann. Geophysicae, **17**, 115–121.

Thorpe, S. A., **1968**, A method of producing shear in a stratified fluid, J. Fluid. Mech., **32**, 693-704.

Tiedtke, M., **1989**: A comprehensive mass flux scheme for cumulus parameterization in large-scale models, Mon. Wea. Rev., **117**: 1779-1799.

Turner, J., **1999**: Development of a mountain wave turbulence prediction scheme for civil aviation, Forecasting research, Technical report, No 265, Meteorological office, Bracknell, UK, 34 pp.

Van der Hoven, I, **1957**: Power spectrum of horizontal wind speed in the frequency range from 0.0007 to 900 cycles per hour, J. Meteor., **14**, 160-164.

Wilks, D. S., **1995**: Statistical Methods in the atmospheric sciences, Academic Press, Inc., San Diego, 467 pp.

Wanta, R. C., **1953**: The onset of turbulence in an elevated layer near sunrise, Quart. J. R. Met. Soc., **79**, 398.

Woods, J. D., **1968**, Wave-induced shear instability in the summer thermocline, J. Fluid. Mech., **32**, 791-800.

Arbeitsbericht

MeteoSchweiz

Arbeitsberichte der MeteoSchweiz

Kürzlich erschienen:

209 Schmutz C, Schmuki D, Duding O, Rohling S: 2004, Aeronautical Climatological Information Sion LSGS, 77pp, 25 Fr.

208 Schmuki D, Schmutz C, Rohling S: 2004, Aeronautical Climatological Information Grenchen LSZG, 73pp, 24 Fr.

207 Moesch M, Zelenka A: 2004, Globalstrahlungsmessungen 1981-2000 im ANETZ, 83pp, 26 Fr.

206 Schmutz C, Schmuki D, Rohling S: 2004, Aeronautical Climatological Information St.Gallen LSZR, 78pp, 25 Fr.

205 Schmutz C, Schmuki D, Ambrosetti P, Gaia M, Rohling S: 2004, Aeronautical Climatological Information Lugano LSZA, 81pp, 26 Fr.

204 Schmuki D, Schmutz C, Rohling S: 2004, Aeronautical Climatological Information Bern LSZB, 80pp, 25 Fr.

203 Duding O, Schmuki D, Schmutz C, Rohling S: 2004, Aeronautical Climatological Information Geneva LSGG, 104pp, 31 Fr.

202 Bader S: 2004, Tropische Wirbelstürme – Hurricanes –Typhoons – Cyclones, 40pp, 16 Fr.

201 Schmutz C, Schmuki D, Rohling S: 2004, Aeronautical Climatological Information Zurich LSZH, 110pp, 34 Fr.

200 Bader S: 2004, Die extreme Sommerhitze im aussergewöhnlichen Witterungsjahr 2003, 25pp, 14 Fr.

199 Frei T, Dössegger R, Galli G, Ruffieux D: 2002, Konzept Messsysteme 2010 von MeteoSchweiz, 100pp, 32 Fr.

198 Kaufmann P: 2002, Swiss Model Simulations for Extreme Rainfall Events on the South Side of the Alps, 40pp, 20 Fr.

197 WRC Davos (Ed): 2001, IPC - IX, 25.9. - 13.10.2000, Davos, Switzerland, 100pp, 32 Fr.

196 Hächler P et al.: 1999, Der Föhnfall vom April 1993, 139pp , 40 Fr.

195 Urfer Ch, Vogt R, 1999, Die Niederschlagsverhältnisse in Basel 1964-1998, 43pp, 40 Fr.

194 Courvoisier HW: 1998, Statistik der 24-stündigen Starkniederschläge in der Schweiz 1901 – 1996, 20pp, 11 Fr.

193 Defila C, Vonderach G: 1998, Todesfälle und Wetterlagen in Schaffhausen, 72pp, 25 Fr.

192 Maurer H: 1997, Frostprognose in der Schweiz: neue Methode mit automatischen Stationen, 38pp, 16 Fr.

191 Schönbächler M: 1996, Objektive Kontrolle der Textprognose SMA OPKO, 31pp, 14 Fr.

190 Brändli J: 1996, Statistische Auswertungen von täglichen und monatlichen Verdunstungswerten an 22 Standorten der Schweiz, 52pp, 19 Fr.

189 Schneiter D: 1994, SMI contribution to ETEX project in 1994, 24 Fr.

188 Fröhlich C: 1996, Internationaler Pyrheliometervergleich Comparison IPC VIII 25 September - 13 October 1995 Results and Symposium, 35 Fr.

187 Calame F: 1996, Evolution de la température de l'air et de la phénologie d'espèces végétales entre 1952 et 1992 dans la région genevoise et sur le Plateau Suisse, 19pp, 11 Fr.

186 Spinedi F, et al.: 1995, Le alluvioni del 1993 sul versante subalpino, 42pp, 20 Fr.

185 Held E: 1995, Radarmessung im Niederschlag und der Einfluss der Orographie, 98pp, 33 Fr.

Frühere *Veröffentlichungen* und *Arbeitsberichte* finden sich unter
www.meteoschweiz.ch

Arbeitsbericht

MeteoSchweiz

Veröffentlichungen der MeteoSchweiz

Kürzlich erschienen:

72 Mathis H: 2005, Impact of Realistic Greenhouse Gas Forcing on Seasonal Forecast Performance, 80pp, 75 Fr.

71 Leuenberger D: 2005, High-Resolution Radar Rainfall Assimilation: Exploratory Studies with Latent Heat Nudging, 103pp, 81 Fr.

70 Müller G und Viatte P: 2005, The Swiss Contribution to the Global Atmosphere Watch Programme – Achievements of the First Decade and Future Prospects, 112pp, 83 Fr.

69 Müller WA: 2004, Analysis and Prediction of the European Winter Climate, 115pp, 34Fr.

68 Bader S: 2004, Das Schweizer Klima im Trend: Temperatur- und Niederschlagsentwicklung seit 1864, 48pp, 18 Fr.

67 Begert M, Seiz G, Schlegel T, Musa M, Baudraz G und Moesch M: 2003, Homogenisierung von Klimamessreihen der Schweiz und Bestimmung der Normwerte 1961-1990, Schlussbericht des Projektes NORM90, 170pp, 40 Fr.

66 Schär Christoph, Binder Peter, Richner Hans (Eds.): 2003, International Conference on Alpine Meteorology and MAP Meeting 2003, Extended Abstracts volumes A and B, 580pp, 100 Fr.

65 Stübi R: 2002, SONDEX / OZEX campaigns of dual ozone sondes flights: Report on the data analysis, 78pp, 27 Fr.

64 Bolliger M: 2002, On the characteristics of heavy precipitation systems observed by Meteosat-6 during the MAP-SOP**,** 116pp, 36 Fr.

63 Favaro G, Jeannet P, Stübi R: 2002, Re-evaluation and trend analysis of the Payerne ozone sounding, 99pp, 33 Fr.

62 Bettems JM: 2001, EUCOS impact study using the limited-area non-hydrostatic NWP model in operational use at MeteoSwiss, 17pp, 12 Fr.

61 Richner H, et al.: 1999, Grundlagen aerologischer Messungen speziell mittels der Schweizer Sonde SRS 400, 140pp, 42 Fr.

60 Gisler O: 1999, Zu r Methodik einer Beschreibung der Entwicklung des linearen Trends der Lufttemperatur über der Schweiz im Zeitabschnitt von 1864 bis 1990**,** 125pp**,** 36 Fr.

59 Bettems J-M**:** 1999, The impact of hypothetical wind profiler networks on numerical weather prediction in the Alpine region**,** 65pp, 25 Fr.

58 Baudenbacher, M: 1997**,** Homogenisierung langer Klimareihen, dargelegt am Beispiel der Lufttemperatur**,** 181pp**,** 50 Fr.

57 Bosshard, W: 1996, Homogenisierung klimatologischer Zeitreihen, dargelegt am Beispiel der relativen Sonnenscheindauer, 136pp, 38 Fr.

56 Schraff, C: 1996, Data Assimilation and Mesoscale Weather Prediction: A Study with a Forecast Model for the Alpine Region, 138pp, 38 Fr.

55 Wolfensberger, H: 1994, Chronik der Totalisatoren, Handbuch zu den Niederschlags-Totalisatoren, 390pp, 78 Fr.

54 Fankhauser, GA: 1993, Einfluss der Witterung auf den Ertrag und die Qualität von Zuckerrübenkulturen, 116pp, 36 Fr.

53 de Montmollin A: 1993, Comparaisons de différentes méthodes de calcul de la température journalière dans leurs influences sur les longues séries d'observations, 144pp, 41 Fr.

Frühere *Veröffentlichungen* und *Arbeitsberichte* finden sich unter
www.meteoschweiz.ch